

Master's Thesis

Second Harmonic Spectroscopy with an Infrared Free-Electron Laser



Fritz-Haber-Institut
der Max-Planck-Gesellschaft

Submitted to the
Department of Physics
Freie Universität Berlin

Christopher Jeffrey Winta

May 12, 2016

1st Supervisor:

Prof. Dr. Martin Wolf

Fritz-Haber-Institut der Max-Planck-Gesellschaft

Department of Physical Chemistry

2nd Supervisor:

PD Dr. Albrecht Lindinger

Freie Universität Berlin

Institute for Experimental Physics

Group Leader:

Dr. Alexander Paarmann

Fritz-Haber-Institut der Max-Planck-Gesellschaft

Department of Physical Chemistry

Declaration of Authorship

I hereby certify that this thesis has been composed by me and is based on my own work, unless stated otherwise. No other person's work has been used without due acknowledgement in this thesis. All references and verbatim extracts have been quoted, and all sources of information, including graphs and data sets, have been specifically acknowledged.

Berlin, May 12, 2016

Christopher Jeffrey Winta

Contents

1. Introduction	1
2. Theoretical Background	3
2.1. Linear Optical Response Near Phonon Resonances	4
2.1.1. Concept of Light-Matter Interaction	4
2.1.2. Effect of Phonon Resonances on the Linear Response . .	5
2.1.3. Fresnel Tensors	8
2.2. Nonlinear Optical Response	11
2.2.1. Nonlinear Susceptibilities	11
2.2.2. Second Harmonic Generation	12
2.3. Properties of Quartz	15
2.3.1. Crystal Structure and Symmetry	15
2.3.2. Phonon Modes	15
2.4. Working Principle of Free-Electron Lasers	18
2.4.1. Basic Setup	18
2.4.2. Synchrotron Radiation in an Undulator	19
2.4.3. Microbunching	21
2.4.4. Cavity Detuning	23
3. Simulations	25
3.1. Dispersion of the Dielectric Function	25
3.2. Reflectivity Spectra	26
3.3. Azimuthal SHG	27
3.3.1. Surface Contribution	30
3.3.2. β -Quartz	32
4. Experimental Setup	33
4.1. The FHI Free-Electron Laser	33
4.1.1. Pulse Structure	34
4.2. The SHG Setup	35
4.2.1. Detection	36
4.2.2. Samples and Probe Heater	37
4.3. Beamline Characterization	37

5. Results	41
5.1. Second Harmonic Phonon Spectroscopy	41
5.1.1. Temperature Dependence of the SHG Spectrum	43
5.2. Probing the Crystal Structure: Azimuthal SHG	45
5.2.1. Temperature Dependence of the Azimuthal Scans	47
5.3. Linear Spectroscopy: Reflectivity	50
5.3.1. Temperature Dependence of the Reflectivity Spectrum	50
6. Discussion	55
6.1. Interpretation of SHG Spectra	55
6.2. Nonlinear vs. Linear Measurements	56
6.3. Anomaly at Ω_6^{TO}	59
6.4. $\alpha \rightarrow \beta$ Phase Transition of Quartz	60
7. Summary & Outlook	61
Appendix A. Gaussian Beams	63
A.1. Description	63
A.2. Beam Parameters	64
A.3. ABCD Law	65
References	67
List of Figures	69
Acknowledgements	73

1. Introduction

First discovered in 1961 [1], second harmonic generation (SHG) is a well-known phenomenon of second-order nonlinear optics. It describes the interaction of two photons with the same energy in a nonlinear, non-centrosymmetric material. These two photons are combined to form one photon of twice the original energy. Despite its wide application in the near-infrared and visible spectral range, very few experiments with SHG have been conducted in the mid- and far-infrared which is mainly due to the scarcity of suitable light sources. The mid- to far-infrared wavelength region itself is highly intriguing, especially for molecular and solid state physics as it includes the so-called molecular fingerprint region where most molecular excitation energies lie as well as Reststrahlen bands of solids ranging from the transverse optical (TO) to the longitudinal optical (LO) phonon frequencies [2]. These Reststrahlen bands exhibit peculiar features as near-perfect reflectivity due to negative values of the dielectric function $\epsilon(\omega)$ [2].

We employ second harmonic phonon spectroscopy in the mid-infrared [3] to study zone-center optical phonons using crystalline quartz (SiO_2) as a model system. This second-order nonlinear spectroscopy has been shown to be highly sensitive to phonon resonances for crystals with broken inversion symmetry [3]. The free-electron laser (FEL) at the Fritz Haber Institute in Berlin (FHI) constitutes an excellent tool to study resonances in the mid-infrared wavelength region of solids. Its wide tuning range (4 μm to 48 μm), narrow linewidth (0.5 % to 5 %) and high peak fields [4] offer promising opportunities for nonlinear spectroscopic applications, especially at sharp resonances. Additionally, for certain crystal symmetries, the second-order nonlinear signal exhibits an azimuthal (rotation about the surface normal) dependence which can be exploited to distinguish different signal contributions.

Quartz is particularly suited as a model system for SHG spectroscopy as it is well studied with vibrational sum frequency generation (SFG) [5, 6], has multiple phonon resonances in the mid-IR and shows a strong azimuthal dependence due to its trigonal crystal symmetry. Additionally, at a temperature of 573 $^\circ\text{C}$ quartz has a phase transition from α -quartz to β -quartz where the material undergoes a change in crystal symmetry from a trigonal to a hexagonal structure. Owing to its nonlinearity, SHG spectroscopy might be sensitive to this phase transition, a question which amongst others is to be addressed in this thesis.

1. Introduction

Using SFG, it has been shown that the strong azimuthal dependence of the bulk signal can be utilized to detect surface contributions [5, 6]. Second harmonic phonon spectroscopy, as an alternative even-order nonlinear technique to SFG, offers particularly high peak sensitivity as it involves a doubly resonant excitation process comparable to stimulated resonant anti-Stokes Raman scattering (see figure 1.1b) while SFG involves a singly resonant process (cf. stimulated nonresonant Raman scattering, see figure 1.1a). Additionally, compared to SFG, SHG lifts the requirement of phonon resonances to be Raman-active in order to be detectable due to additional terms entering the nonlinear susceptibility tensor $\chi^{(2)}$ [3].

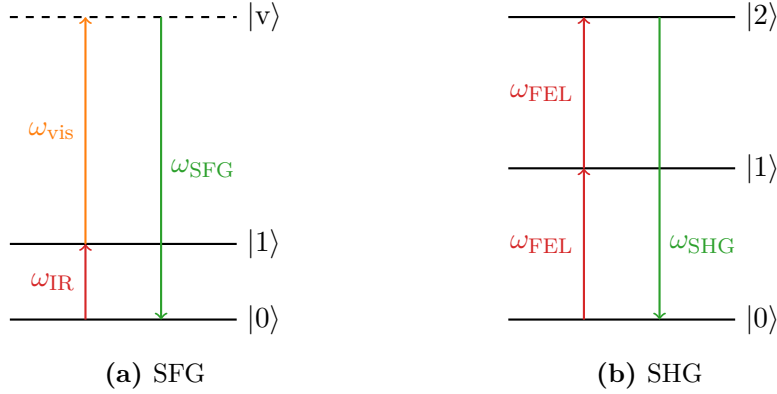


Figure 1.1. Energy diagrams for (a) sum frequency generation and (b) second harmonic generation. Energy levels $|0\rangle$, $|1\rangle$ and $|2\rangle$ indicate resonant transitions while $|v\rangle$ is a virtual state.

Apart from non-centrosymmetric materials, second harmonic spectroscopy can also be applied to materials with inversion symmetry to study surfaces and interfaces where the inversion symmetry of the crystal is broken.

This thesis is divided into six main parts. The first chapter, this introduction, is followed by the theoretical basics which cover the physical concepts necessary to understand the SHG experiment and the calculations done for this work. The third chapter deals with the SHG setup itself, giving experimental details including a short overview of the FEL's main features, a detailed description of the autocorrelator setup used to measure SHG spectra as well as a characterization of the sample. The results of the conducted measurements are presented in chapter four and discussed in chapter five. Finally, a short prospect for possible future experiments and measurements is given as well as ideas to improve the existing setup.

2. Theoretical Background

This chapter covers the theoretical concepts of this work and introduces models of nonlinear optics to describe the processes involved in second harmonic spectroscopy.

The SHG intensity is generally given by:

$$I_{\text{SHG}} \propto \left| \chi^{(2)}(\omega) \mathbf{E}(\omega)^2 \right|^2 \quad (2.0.1)$$

where $\chi^{(2)}(\omega)$ is the second-order nonlinear susceptibility and $\mathbf{E}(\omega)$ the local electric field. According to equation 2.0.1, these two dispersive quantities determine the generated SH signal. Thus, they need to be characterized in order to simulate SHG spectra.

Thereeto, the first section of this chapter covers the concept of light-matter interaction introducing the linear $\chi^{(1)}(\omega)$ tensor and describing a material's linear response in the form of an electric polarization $\mathbf{P}(\omega)$. The electric susceptibility $\chi(\omega)$ is directly related to the dielectric function $\varepsilon(\omega)$ which itself depends on phonon resonances in the material and thus describes their effect on the optical response. Finally, a derivation of the Fresnel transmission and reflection coefficients is given which allow for a calculation of the local electric fields $\mathbf{E}(\omega)$, depending on the incident fields, the angle of incidence and the material's response given by $\varepsilon(\omega)$.

The second section extends the described linear model by nonlinear susceptibilities which govern higher-order nonlinear optical effects. The anharmonic oscillator model is introduced which explains the occurrence of higher harmonics, including second harmonic generation. A model for the dispersion of the second-order nonlinear susceptibility $\chi^{(2)}(\omega)$ is presented as well as SHG-specific symmetry considerations.

The third section lays out some general properties of α -quartz including its crystal structure and symmetry as well as its phase transition to β -quartz. Also, temperature-dependent phonon mode data is given.

Finally, the fourth section treats the working principle of free-electron lasers which generate light by injecting relativistically moving electrons into a periodic array of permanent magnets. These electrons emit synchrotron radiation which then interacts with the electron beam, resulting in a mechanism that is analogous to stimulated emission for conventional lasers. Additionally, the effect of cavity detuning, i.e. adjustment of the cavity length relative to the emitted wavelength, is discussed.

2.1. Linear Optical Response Near Phonon Resonances

This section covers definitions and fundamental concepts of a medium's linear optical response to an external electric field \mathbf{E}_{ext} . It discusses the material's response due to the applied field which is described by the so-called constitutive equation as well as the emission of an electric field \mathbf{E}_{em} caused by the induced polarization which follows Maxwell's equations. The theoretical groundwork is mainly taken from Yuen-Ron Shen's *"The Principles of Nonlinear Optics"* [7] and also draws from Guang S. He's and Song H. Liu's *"Physics of Nonlinear Optics"* [8].

2.1.1. Concept of Light-Matter Interaction

Since we intend to describe the optical response of a medium, it is essential to consider Maxwell's equations which describe the formation of electric and magnetic fields, $\mathbf{E}(\mathbf{r}, t)$ and $\mathbf{B}(\mathbf{r}, t)$, and govern all electromagnetic phenomena [9]:

$$\begin{aligned}\nabla \times \mathbf{E} &= -\frac{1}{c} \frac{\partial \mathbf{B}}{\partial t}, \\ \nabla \times \mathbf{B} &= \frac{1}{c} \frac{\partial \mathbf{E}}{\partial t} + \frac{4\pi}{c} \mathbf{J}, \\ \nabla \cdot \mathbf{E} &= 4\pi\rho, \\ \nabla \cdot \mathbf{B} &= 0\end{aligned}\tag{2.1.1}$$

where $\mathbf{J}(\mathbf{r}, t)$ and $\rho(\mathbf{r}, t)$ denote, respectively, the current and charge densities. By applying an external electric field $\mathbf{E}_{\text{ext}}(\mathbf{r}, t)$ to the medium, e.g. using lasers, it is possible to induce current and charge densities, $\mathbf{J}(\mathbf{r}, t)$ and $\rho(\mathbf{r}, t)$, which itself, following Maxwell's equations 2.1.1, can cause emission of a secondary electric field $\mathbf{E}(\mathbf{r}, t)$. Therefore, $\mathbf{J}(\mathbf{r}, t)$ and $\rho(\mathbf{r}, t)$ are said to act as source terms.

In nonlinear optics, it is often convenient to relate $\mathbf{J}(\mathbf{r}, t)$ to $\rho(\mathbf{r}, t)$ using the law of charge conservation,

$$\nabla \cdot \mathbf{J} + \frac{\partial \rho}{\partial t} = 0,\tag{2.1.2}$$

and to define a generalized electric polarization $\mathbf{P}(\mathbf{r}, t)$:

$$\mathbf{J} = \mathbf{J}_{\text{dc}} + \frac{\partial \mathbf{P}}{\partial t}\tag{2.1.3}$$

where \mathbf{J}_{dc} is the dc current density. Now, by applying equations 2.1.2 and 2.1.3 to the third and second equation of 2.1.1, respectively, Maxwell's equations can

be written as:

$$\begin{aligned}\nabla \times \mathbf{E} &= -\frac{1}{c} \frac{\partial \mathbf{B}}{\partial t}, \\ \nabla \times \mathbf{B} &= \frac{1}{c} \frac{\partial}{\partial t}(\mathbf{E} + 4\pi\mathbf{P}) + \frac{4\pi}{c} \mathbf{J}_{\text{dc}}, \\ \nabla \cdot (\mathbf{E} + 4\pi\mathbf{P}) &= 0, \\ \nabla \cdot \mathbf{B} &= 0\end{aligned}\tag{2.1.4}$$

with $\mathbf{P}(\mathbf{r}, t)$ being the only remaining time-varying source term [7]. The generalized electric polarization $\mathbf{P}(\mathbf{r}, t)$ appears as a nonlocal function which depends on \mathbf{r} . For all practical purposes in this thesis, the position dependency can be dropped as the wavelengths of the used radiation are much larger than the atomic radii, thus the electric dipole approximation applies and therefore $\mathbf{P}(\mathbf{r}, t) = \mathbf{P}(t)$ and $\mathbf{E}_{\text{ext}}(\mathbf{r}, t) = \mathbf{E}_{\text{ext}}(t)$.

In general, $\mathbf{P}(t)$ depends on the applied electric field $\mathbf{E}_{\text{ext}}(t)$ and completely describes the medium's response to an external electric field. The relation between $\mathbf{P}(t)$ and $\mathbf{E}_{\text{ext}}(t)$ is known as the constitutive equation which in the linear case takes the form [10]:

$$\mathbf{P}(t) = \int_{-\infty}^{\infty} \chi^{(1)}(t - t') \cdot \mathbf{E}_{\text{ext}}(t') dt' \tag{2.1.5}$$

where $\chi^{(1)}$ is the linear susceptibility tensor and integrating over dt' accounts for the fact that the medium's optical response to an external electric field is in general not instantaneous.

If the external electric field is a monochromatic plane wave,

$$\mathbf{E}_{\text{ext}}(t) = \mathbf{E}_{\text{ext}}(\omega) = \mathcal{E}_{\text{ext}}(\omega) e^{-i\omega t}, \tag{2.1.6}$$

then Fourier transform of equation 2.1.5 yields [7]:

$$\begin{aligned}\mathbf{P}(t) &= \mathbf{P}(\omega) = \chi^{(1)}(\omega) \cdot \mathbf{E}_{\text{ext}}(\omega) \\ \text{with } \chi^{(1)}(\omega) &= \int_{-\infty}^{\infty} \chi^{(1)}(t) e^{i\omega t} dt.\end{aligned}\tag{2.1.7}$$

2.1.2. Effect of Phonon Resonances on the Linear Response

The dielectric function $\varepsilon(\omega)$ of a material describes, like the susceptibility $\chi(\omega)$, the material's response to an external electric field. In fact, both quantities are related via:

$$\varepsilon(\omega) = 1 + \chi(\omega). \tag{2.1.8}$$

$\varepsilon(\omega)$ acts as a proportionality constant which connects the external electric field $\mathbf{E}(\omega)$ with an electric displacement vector $\mathbf{D}(\omega) = \mathbf{E}(\omega) + \mathbf{P}(\omega) = \varepsilon(\omega)\mathbf{E}(\omega)$. For nonresonant interactions, it is a purely real quantity, while for resonant interactions, an imaginary component arises due to absorption losses [11]. Therefore,

$$\varepsilon(\omega) = \varepsilon_1 + i\varepsilon_2 \tag{2.1.9}$$

2. Theoretical Background

where ε_1 is a measure of the material's response in terms of electronic displacement (and thus polarization) and ε_2 is a measure of absorption in the material.

For dielectrics in the wavelength region well below electronic resonances, the linear response described via $\varepsilon(\omega)$ originates from two sources: the electronic and the ionic response of the material which can be expressed as:

$$\varepsilon(\omega) = 1 + \chi_\infty + \chi_{\text{ion}}(\omega) \quad (2.1.10)$$

where χ_∞ holds the electronic and χ_{ion} the ionic contributions. Ionic, i.e. phonon resonances lie well below electronic resonances, thus for the spectral region of phonon resonances, χ_∞ can be considered as the high-frequency limit and therefore practically constant, while the ionic contribution $\chi_{\text{ion}}(\omega)$ can be expressed as [12]:

$$\chi_{\text{ion}}(\omega) = \frac{S\Omega_{\text{TO}}^2}{\Omega_{\text{TO}}^2 - \omega^2 - i\gamma\omega} \quad (2.1.11)$$

where $\Omega_{\text{TO(LO)}}$ and $\gamma_{\text{TO(LO)}}$ are the frequencies of the TO (LO) phonon, γ the phonon damping and $S = \varepsilon_\infty(\Omega_{\text{LO}}^2 - \Omega_{\text{TO}}^2)/\Omega_{\text{TO}}^2$ the oscillator strength [12]. This, together with equation 2.1.10, results in an expression for the dielectric function:

$$\varepsilon(\omega) = \varepsilon_\infty \left(1 + \frac{\Omega_{\text{LO}}^2 - \Omega_{\text{TO}}^2}{\Omega_{\text{TO}}^2 - \omega^2 - i\gamma\omega} \right) \quad (2.1.12)$$

with $\varepsilon_\infty = 1 + \chi_\infty$. Invoking the Lydanne-Sachs-Teller relation [13] which connects the TO and LO phonon frequencies with the dielectric constants ε_{st} , i.e. the low-frequency limit of $\varepsilon(\omega)$, and ε_∞ and reads:

$$\frac{\varepsilon_{\text{st}}}{\varepsilon_\infty} = \left(\frac{\Omega_{\text{LO}}}{\Omega_{\text{TO}}} \right)^2, \quad (2.1.13)$$

gives:

$$\varepsilon(\omega) = \varepsilon_\infty \left(\frac{\Omega_{\text{LO}}^2 - \omega^2 + i\gamma_{\text{LO}}\omega}{\Omega_{\text{TO}}^2 - \omega^2 - i\gamma_{\text{TO}}\omega} \right). \quad (2.1.14)$$

From this form, it is apparent that the LO phonon frequency marks the zero-crossing of the real part of $\varepsilon(\omega)$ (numerator becomes zero) and that $\varepsilon(\omega)$ peaks at the TO phonon frequency (denominator becomes zero).

It has been shown that for multiple resonances, equation 2.1.14 can be written in its factorized form [14, 15]:

$$\varepsilon(\omega) = \varepsilon_\infty \prod_j \frac{\Omega_{j,\text{LO}}^2 - \omega^2 + i\gamma_{j,\text{LO}}\omega}{\Omega_{j,\text{TO}}^2 - \omega^2 - i\gamma_{j,\text{TO}}\omega} \quad (2.1.15)$$

where $\Omega_{j,\text{TO(LO)}}$ marks the j th TO (LO) phonon frequency and $\gamma_{j,\text{TO(LO)}}$ its respective damping.

The dielectric function around a phonon mode is plotted together with its refractive index $\tilde{n} = \sqrt{\varepsilon(\omega)}$ in figure 2.1a and 2.1b using equation 2.1.15. The real part of $\varepsilon(\omega)$ is negative between the TO and its corresponding LO phonon

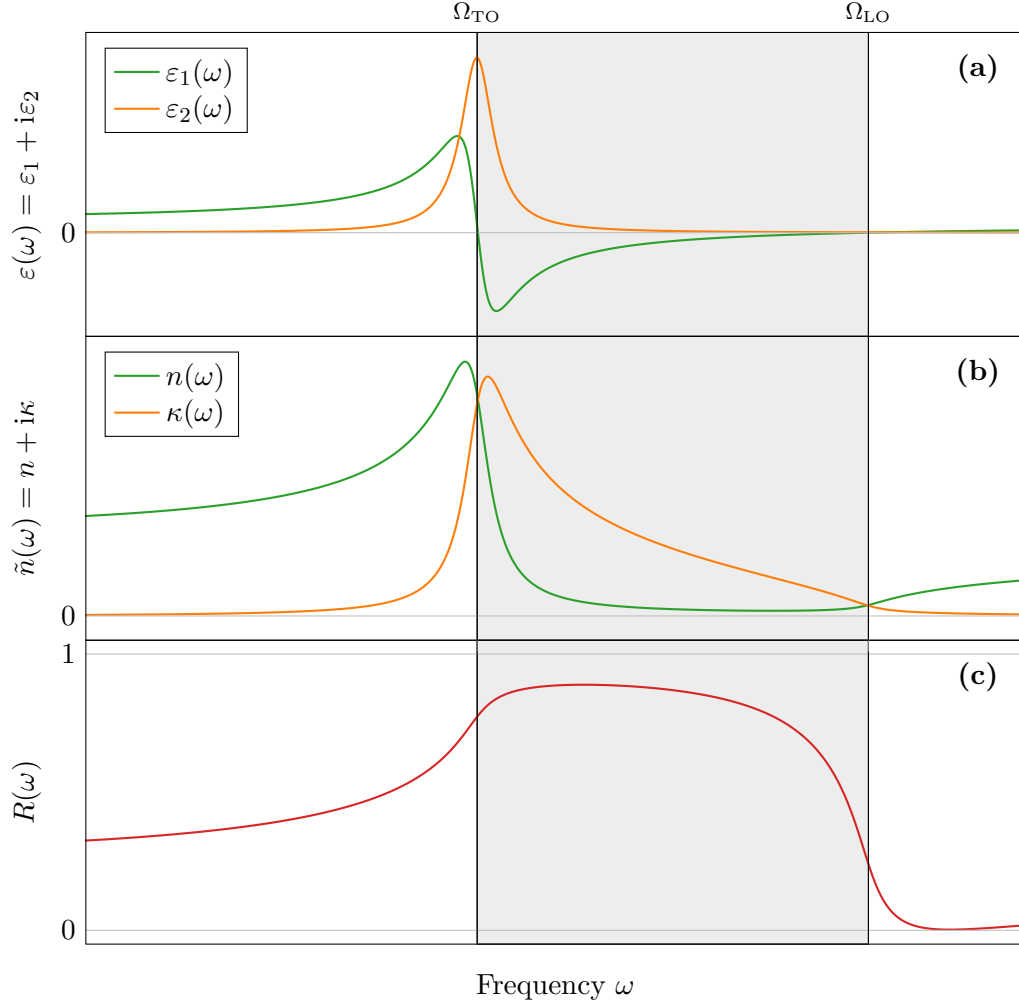


Figure 2.1. (a): Dielectric function $\varepsilon(\omega)$ around a phonon resonance. The real part crosses zero at the LO phonon frequency while the imaginary part peaks at the TO phonon frequency. The spectral region between corresponding TO and LO frequencies is known as the Reststrahlen band (gray shade) and exhibits near-perfect reflectivity. (b): Refractive index $\tilde{n} = n + i\kappa$. (c): Reflectivity R according to equation 2.1.16.

2. Theoretical Background

frequency, resulting in an inversely phased polarization inside the crystal with respect to the driving field and thus a screening of the radiation. As the radiation cannot propagate inside the crystal, this spectral region is of particularly high reflectance and is known as the *Reststrahlen* (German: residual rays) band.

It can be shown that the imaginary part takes the form of a Lorentzian about the TO phonon frequency Ω_{TO} [12] and that the real part crosses zero at the LO frequency Ω_{LO} [11].

For a purely real dielectric function $\varepsilon(\omega)$ and normal incidence of the incoming beam, the fraction of the reflected power, i.e. the reflectivity R , is given by [16]:

$$R = \left| \frac{\sqrt{\varepsilon(\omega)} - 1}{\sqrt{\varepsilon(\omega)} + 1} \right|^2. \quad (2.1.16)$$

and plotted in figure 2.1c. For a non-normal angle of incidence, the Fresnel coefficients of reflection need to be considered which are covered in the following section.

2.1.3. Fresnel Tensors

The Fresnel coefficients of transmission and reflection govern the relation between the external electric field and the local electric field in the material and the electric field of the reflected beam, respectively. They are of particular importance for this work as they affect SHG spectra as well as reflectivity spectra and allow for angle-dependent calculations while taking spectral resonances in the material into account. For an anisotropic material as the studied sample, those Fresnel coefficients take the form of second rank diagonal tensors [16] whose non-vanishing elements are to be calculated in this section.

In the following expressions, \mathbf{k} denotes the complex wave vectors, \mathbf{E} the electric fields, \mathbf{H} the magnetic fields and α the angles of incidence with indices i, r and t for the incoming, reflected and transmitted beam, respectively. For simplicity, these calculations are restricted to materials whose optic axis c is perpendicular to the sample's surface as is the case for the studied sample. Without loss of generality, the surface normal is defined along the z -axis and the plane of incidence along the x - z -plane as shown in figure 2.2.

Transmission Coefficients

We will carry out this derivation of the Fresnel transmission coefficients for P-polarized light first (as depicted in figure 2.2). The results for S-polarized light can be obtained analogously and will be given at the end of this section.

In order to calculate the non-zero components of the Fresnel transmission tensor, we need to invoke Maxwell's equations in the following manner:

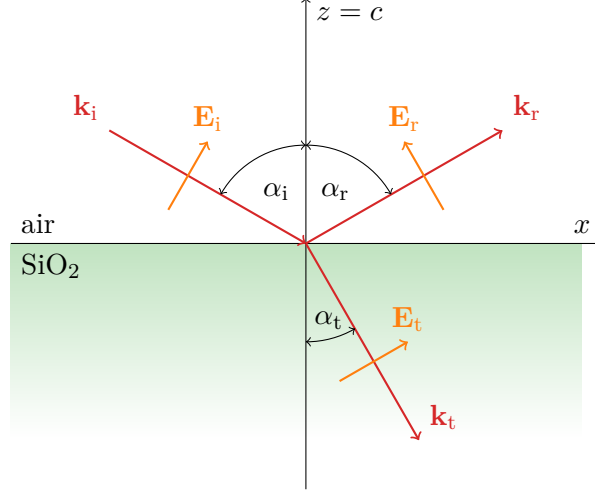


Figure 2.2. Schematic of wave vectors \mathbf{k} for reflection/transmission of light on/through quartz (SiO₂), also indicating electric field vectors \mathbf{E} for P-polarization. For the α -quartz c -cut, the optic axis c is parallel to the z -axis, i.e. perpendicular to the sample's surface.

$$\begin{aligned} \nabla \times \mathbf{H} = \varepsilon \frac{\partial \mathbf{E}}{\partial t} : \quad k_{t,z} H_{t,y} = 2\pi\omega \varepsilon_x E_{t,x} &\rightarrow E_{t,x} = \frac{1}{2\pi\omega \varepsilon_x} k_{t,z} H_{t,y}, \\ -k_{t,x} H_{t,y} = 2\pi\omega \varepsilon_z E_{t,z} &\rightarrow E_{t,z} = -\frac{1}{2\pi\omega \varepsilon_z} k_{t,x} H_{t,y} \end{aligned} \quad (2.1.17)$$

$$\begin{aligned} \nabla \times \mathbf{E} = -\mu \frac{\partial \mathbf{H}}{\partial t} : \quad k_{i,x} E_{i,z} - k_{i,z} E_{i,x} = -2\mu\pi\omega H_{i,y} \\ \xrightarrow{\mu=1} H_{i,y} = -\frac{1}{2\pi\omega} (k_{i,x} E_{i,z} - k_{i,z} E_{i,x}) \end{aligned} \quad (2.1.18)$$

where \mathbf{E} and \mathbf{H} are each proportional to $e^{i(\mathbf{k}\mathbf{r}-\omega t)}$ and $\mu = 1$ for non-magnetic materials. ε_x and ε_z denote the x - and z -components of the dielectric function, respectively.

Next, we can utilize the conservation of tangential components of the electric field at interfaces as a boundary condition to find an expression for the magnetic field $H_{t,y}$ inside the material:

$$E_{i,x} + E_{r,x} = E_{t,x} \quad (2.1.19)$$

as there is no y -component of the electric field for P-polarization. Plugging in $k_z H_y = \omega \varepsilon_x E_x$ (cf. first equation of 2.1.17) and using $k_{i,z} = -k_{r,z}$ as well as the conservation of tangential magnetic field components, $H_{i,y} + H_{r,y} = H_{t,y}$, then yields:

$$H_{t,y} = \frac{2\varepsilon_x k_{i,z}}{\varepsilon_x k_{i,z} + \varepsilon_0 k_{t,z}} H_{i,y} \equiv F H_{i,y} \quad (2.1.20)$$

2. Theoretical Background

where ε_0 is the dielectric constant of air which can be set to 1. From trigonometrical considerations and Snell's law of refraction, an expression for $k_{t,z}$ can be obtained [17]:

$$k_{t,z,e} = 2\pi\omega \sqrt{\varepsilon_x - \frac{\varepsilon_x}{\varepsilon_z} \sin^2 \alpha_i} \quad (2.1.21)$$

where the additional subscript e stands for extraordinary (i.e. polarization parallel to optic axis) which is a property of P-polarized electromagnetic waves traveling along the z -direction as opposed to S-polarized electromagnetic waves traveling along the y -direction which are purely ordinary (i.e. polarization perpendicular to optic axis, subscript o). Using expressions 2.1.20 and 2.1.21 and inserting them into 2.1.17 yields:

$$\begin{aligned} E_{t,x} &= \frac{1}{(2\pi)^2 \omega^2 \varepsilon_x} k_{t,z,e} F(k_{i,z} E_{i,x} - k_{i,x} E_{i,z}) \\ E_{t,z} &= -\frac{1}{(2\pi)^2 \omega^2 \varepsilon_z} k_{t,x} F(k_{i,z} E_{i,x} - k_{i,x} E_{i,z}). \end{aligned} \quad (2.1.22)$$

Simple trigonometry ($k_{i,x} = 2\pi\omega \sin \alpha_i$, $k_{i,z} = 2\pi\omega \cos \alpha_i$, $E_{i,x} = E_i \cos \alpha_i$ and $E_{i,z} = -E_i \sin \alpha_i$, see figure 2.2) and plugging in the definition of F gives:

$$\begin{aligned} E_{t,x} &= \frac{k_{t,z}}{2\pi\omega \varepsilon_x} F E_i = \frac{k_{t,z}}{2\pi\omega \varepsilon_x} \frac{2\varepsilon_x k_{i,z}}{\varepsilon_x k_{i,z} + \varepsilon_0 k_{t,z}} E_i \\ E_{t,z} &= -\frac{k_{t,x}}{2\pi\omega \varepsilon_z} F E_i = \frac{k_{t,x}}{2\pi\omega \varepsilon_z} \frac{2\varepsilon_x k_{i,z}}{\varepsilon_x k_{i,z} + \varepsilon_0 k_{t,z}} E_i. \end{aligned} \quad (2.1.23)$$

With $k_{i,z} E_0 = 2\pi\omega E_{i,x}$ and $k_{t,x} E_0 = -2\pi\omega E_{i,z}$, we finally get [18]:

$$\begin{aligned} E_{t,x} &= \frac{\varepsilon_x}{\varepsilon_x} \frac{2k_{t,z,e}}{\varepsilon_x k_{i,z} + \varepsilon_0 k_{t,z,e}} E_{i,x} \equiv L_{xx} E_{i,x} \\ E_{t,z} &= \frac{\varepsilon_x}{\varepsilon_z} \frac{2k_{i,z}}{\varepsilon_x k_{i,z} + \varepsilon_0 k_{t,z,e}} E_{i,z} \equiv L_{zz} E_{i,z} \end{aligned} \quad (2.1.24)$$

where L_{xx} and L_{zz} are the Fresnel transmission coefficients.

In order to get the corresponding expression for L_{yy} , we must consider S-polarized light by replacing equation 2.1.21 with [17]:

$$k_{t,z,o} = 2\pi\omega \sqrt{\varepsilon_x - \sin^2 \alpha_i}. \quad (2.1.25)$$

Using tangential **H**-field conservation (as opposed to **E**-field conservation for P-polarization) and applying equation 2.1.18 to S-polarized beams, gives analogously:

$$\frac{1}{2\pi\omega} k_{i,z} (E_{i,y} - E_{r,y}) = k_{t,z} E_{t,y}. \quad (2.1.26)$$

Replacing $E_{r,y}$ by $2E_{i,y} - E_{t,y}$ (tangential **E**-field conservation) then yields:

$$E_{t,y} = \frac{2k_{i,z}}{k_{t,z,o} + k_{i,z}} E_{i,y} \equiv L_{yy} E_{i,y}. \quad (2.1.27)$$

Reflection Coefficients

In an analog fashion, the Fresnel reflection coefficients can be derived, leading to the following expressions:

$$\begin{aligned} R_{xx} &= -\frac{\varepsilon_x k_{i,z} - k_{t,z,e}}{\varepsilon_x k_{i,z} + k_{t,z,e}} \\ R_{zz} &= \frac{\varepsilon_x k_{i,z} - k_{t,z,e}}{\varepsilon_x k_{i,z} + k_{t,z,e}} \\ R_{yy} &= \frac{k_{i,z} - k_{t,z,o}}{k_{i,z} + k_{t,z,o}} \end{aligned} \quad (2.1.28)$$

where $k_{t,z,e}$ and $k_{t,z,o}$ are given by equations 2.1.21 and 2.1.25, respectively.

2.2. Nonlinear Optical Response

In this section, the already established linear model of the optical response (see section 2.1) is extended to nonlinear responses in the material, introducing the second-order nonlinear susceptibility $\chi^{(2)}$ which governs, among other nonlinear optical effects, second harmonic generation.

2.2.1. Nonlinear Susceptibilities

Since the polarization $\mathbf{P}(t)$, previously described for the linear case (cf. equation 2.1.7), is usually a complicated nonlinear function of $\mathbf{E}(t)$, it is customary to expand the polarization in terms of powers of the electric field, given that the latter is sufficiently weak:

$$\begin{aligned} \mathbf{P}(t) &= \int_{-\infty}^{\infty} \chi^{(1)}(t - t') \cdot \mathbf{E}(t') dt' \\ &+ \int_{-\infty}^{\infty} \chi^{(2)}(t - t_1, t - t_2) : \mathbf{E}(t_1) \mathbf{E}(t_2) dt_1 dt_2 \\ &+ \int_{-\infty}^{\infty} \chi^{(3)}(t - t_1, t - t_2, t - t_3) : \mathbf{E}(t_1) \mathbf{E}(t_2) \mathbf{E}(t_3) dt_1 dt_2 dt_3 \\ &+ \dots \end{aligned} \quad (2.2.1)$$

where $\chi^{(n)}$ is a tensor of order $(n + 1)$ and denotes the n th-order nonlinear susceptibility tensor and $\cdot (:) :$ indicates tensor multiplication with the electric field(s).

If the electric field $\mathbf{E}(t)$ is a group of plane waves with discrete frequencies ω_i ,

$$\mathbf{E}(t) = \sum_i \mathbf{E}(\omega_i) = \sum_i \mathcal{E}(\omega_i) e^{-i\omega_i t}, \quad (2.2.2)$$

then, analogous to the linear case of equation 2.1.7, Fourier transform of equa-

2. Theoretical Background

tion 2.2.1 yields:

$$\begin{aligned}
\mathbf{P}(\omega) = & \chi^{(1)}(\omega) \cdot \mathbf{E}(\omega) \\
& + \chi^{(2)}(\omega_1, \omega_2, \pm\omega_1 \pm \omega_2) : \mathbf{E}(\omega_1) \mathbf{E}(\omega_2) \\
& + \chi^{(3)}(\omega_1, \omega_2, \omega_3, \pm\omega_1 \pm \omega_2 \pm \omega_3) : \mathbf{E}(\omega_1) \mathbf{E}(\omega_2) \mathbf{E}(\omega_3) \\
& + \dots
\end{aligned} \tag{2.2.3}$$

$$\begin{aligned}
\text{with } \chi^{(n)}(\omega = \omega_1 + \omega_2 + \dots + \omega_n) \\
= \int_{-\infty}^{\infty} \chi^{(n)}(t - t_1; \dots; t - t_n) \\
\times e^{i[\omega_1(t-t_1) + \dots + \omega_n(t-t_n)]} dt_1 \dots dt_n.
\end{aligned}$$

If the linear and nonlinear susceptibilities $\chi^{(n)}$ are known, it is in principle possible to predict the medium's response including all optical effects of order n using Maxwell's equations. Typical examples of second-order optical effects are sum- and difference-frequency generation (SFG, DFG), electro-optic rectification (EOR) as well as second harmonic generation (SHG) whereas third harmonic generation (THG) and self-focusing are processes in $\chi^{(3)}$.

2.2.2. Second Harmonic Generation

Anharmonic Oscillator Model

In order to understand why second-order nonlinear effects like sum- and difference-frequency generation as well as optical rectification occur, it is highly instructive to consider the anharmonic oscillator model.

The model comprises N classical anharmonic oscillators per unit volume which describe electrons bound to the atomic nuclei of the material. In the presence of a driving force, their equation of motion reads:

$$\frac{d^2x}{dt^2} + \Gamma \frac{dx}{dt} + \omega_0^2 x + ax^2 = F \tag{2.2.4}$$

where the driving force F is assumed to originate from two applied oscillating electric fields $\mathbf{E}_{1(2)}$ with Fourier components at $\pm\omega_{1(2)}$ which act on the electrons (charge e , mass m):

$$F = \frac{e}{m} \left[E_1 \left(e^{-i\omega_1 t} + e^{i\omega_1 t} \right) + E_2 \left(e^{-i\omega_2 t} + e^{i\omega_2 t} \right) \right]. \tag{2.2.5}$$

As a result of the applied electric fields, the induced polarization takes the form:

$$\mathbf{P} = Nex. \tag{2.2.6}$$

The anharmonic term ax^2 in equation 2.2.4 is assumed to be small and can therefore be treated as a perturbation with:

$$x = x^{(1)} + x^{(2)} + x^{(3)} + \dots \tag{2.2.7}$$

In this approximation, the first-order solution is obtained by linearizing equation 2.2.4, i.e. setting $ax^2 = 0$, and reads [7]:

$$x^{(1)} = \frac{e}{m} \left[\frac{E_1}{(\omega_0^2 - \omega_1^2 - i\omega_1\Gamma)} e^{-i\omega_1 t} + \frac{E_2}{(\omega_0^2 - \omega_2^2 - i\omega_2\Gamma)} e^{-i\omega_2 t} \right] + \text{c.c.} \quad (2.2.8)$$

where c.c. is the complex conjugate of prior terms. This first-order solution can then be used to obtain a second-order solution by approximating $ax^2 = ax^{(1)2}$. Solving the differential equation 2.2.4 for $x^{(2)}$ then yields [7]:

$$\begin{aligned} x^{(2)} = & x^{(2)}(\omega_1 + \omega_2) + x^{(2)}(\omega_1 - \omega_2) \\ & + x^{(2)}(2\omega_1) + x^{(2)}(2\omega_2) + x^{(2)}(0) + \text{c.c.} \quad \text{with} \\ x^{(2)}(\omega_1 \pm \omega_2) = & \frac{-2a(e/m)^2 E_1 E_2}{(\omega_0^2 - \omega_1^2 - i\omega_1\Gamma)(\omega_0^2 - \omega_2^2 \mp i\omega_2\Gamma)} \\ & 1 \times \frac{1}{\omega_0^2 - (\omega_1 \pm \omega_2)^2 - i(\omega_1 \pm \omega_2)\Gamma} e^{-i(\omega_1 \pm \omega_2)t}, \end{aligned} \quad (2.2.9)$$

$$x^{(2)}(2\omega_i) = \frac{-a(e/m)^2 E_i^2}{(\omega_0^2 - \omega_i^2 - i\omega_i\Gamma)^2 (\omega_0^2 - 4\omega_i^2 - 2i\omega_i\Gamma)} e^{-i2\omega_i t}, \quad i = 1, 2,$$

$$x^{(2)}(0) = -a \left(\frac{e}{m} \right)^2 \frac{1}{\omega_0^2} \left(\frac{1}{\omega_0^2 - \omega_1^2 - i\omega_1\Gamma} + \frac{1}{\omega_0^2 - \omega_2^2 - i\omega_2\Gamma} \right).$$

Equation 2.2.9 clearly shows that new frequency components of the polarization, i.e. $\omega_1 \pm \omega_2$, $2\omega_1$, $2\omega_2$ and 0, arise from the second-order solution which appear due to quadratic interaction of the electric fields [7]. This solution already explains the occurrence of second-order nonlinear effects like sum and difference frequency generation ($\omega = \omega_1 \pm \omega_2$), second harmonic generation ($\omega = 2\omega_i$) as well as optical rectification ($\omega = 0$). Higher-order solutions can be obtained iteratively and predict frequency components at $\omega = n_1\omega_1 + n_2\omega_2$ with $n_1, n_2 \in \mathbb{N}$, giving rise to higher-order nonlinear effects like frequency tripling [7].

Dispersion of the Second-Order Nonlinear Susceptibility

Flytzanis [19] extended the theory of Faust and Henry [20, 21] to calculate the dispersion of $\chi^{(2)}$ for the case that all frequencies involved in the second-order process are below or near a phonon resonance by considering higher-order moments of the polarization and the lattice potential [22]. These calculations presume a zincblende semiconductor with a single phonon mode. According to

2. Theoretical Background

Flytzanis, the second-order nonlinear susceptibility is then given by [19]:

$$\begin{aligned} \chi^{(2)}(\omega_1 + \omega_2, \omega_1, \omega_2) = & \chi_\infty^{(2)} \left[1 + C_1 \left(\frac{1}{D(\omega_1)} + \frac{1}{D(\omega_2)} + \frac{1}{D(\omega_1 + \omega_2)} \right) \right. \\ & + C_2 \left(\frac{1}{D(\omega_1)D(\omega_2)} + \frac{2}{D(\omega_1)D(\omega_1 + \omega_2)} + \frac{1}{D(\omega_2)D(\omega_1 + \omega_2)} \right) \\ & \left. + C_3 \left(\frac{1}{D(\omega_1)D(\omega_2)D(\omega_1 + \omega_2)} \right) \right] \end{aligned} \quad (2.2.10)$$

where $\chi_\infty^{(2)}$ denotes the non-resonant, high frequency second-order electric susceptibility and $D(\omega) = 1 - \omega^2/\omega_{\text{TO}}^2 - i\gamma\omega/\omega_{\text{TO}}^2$ the resonant denominator with the resonant TO phonon frequency ω_{TO} and its damping γ . The parameters C_1 , C_2 and C_3 denote the Faust-Henry parameter [20], electrical and mechanical anharmonicity [19, 23], respectively, and are related to microscopic properties of the medium. These are defined as [23]:

$$\begin{aligned} C_1 &= \frac{\alpha_{\text{TO}}}{2v\chi_\infty^{(2)}} \left(\frac{Z^*}{M\omega_{\text{TO}}^2} \right), \\ C_2 &= \frac{\mu^{(2)}}{2v\chi_\infty^{(2)}} \left(\frac{Z^*}{M\omega_{\text{TO}}^2} \right)^2, \\ C_3 &= -\frac{\phi^{(3)}}{2v\chi_\infty^{(2)}} \left(\frac{Z^*}{M\omega_{\text{TO}}^2} \right)^3 \end{aligned} \quad (2.2.11)$$

where v is the volume of the primitive cell, M the reduced mass, Z^* the effective charge, α_{TO} the TO Raman polarizability per primitive cell, $\mu^{(2)}$ the second-order dipole moment and $\phi^{(3)}$ the third-order lattice potential. From equation 2.2.10 it becomes clear that at phonon resonances the second-order electric susceptibility $\chi^{(2)}$ is drastically enhanced as the denominator $D(\omega)$ approaches zero.

For materials with multiple phonon resonances like quartz, equation 2.2.10 has to be modified. For a complete description of a multi-resonant $\chi^{(2)}$, resonant denominators $D(\omega)$ for all n phonon frequencies have to be taken into account. This results in n different Faust-Henry terms with coefficients $C_{1,1}, \dots, C_{1,n}$ as well as C_2 and C_3 terms describing the electrical and mechanical anharmonicities including all possible cross-terms, i.e. combinations of different phonon modes.

Symmetry Properties

Generally, there are 27 elements of the second-order nonlinear susceptibility tensor $\chi^{(2)}$. These can be reduced by considering structural symmetries of the medium which also should emerge in the optical properties in a certain manner.

Assuming a group of certain symmetry operations $\{S\}$ under which the medium is invariant and therefore $\chi^{(2)}$ remains unchanged, leads to the relation [7]:

$$(\hat{\mathbf{i}} \cdot S^\dagger) \cdot \chi^{(2)} : (S \cdot \hat{\mathbf{j}})(S \cdot \hat{\mathbf{k}}) = \chi_{ijk}^{(2)} \quad (2.2.12)$$

for each symmetry operation S where $\hat{\mathbf{i}}$, $\hat{\mathbf{j}}$ and $\hat{\mathbf{k}}$ refer to the three principle axes of the crystal. The first subscript of $\chi_{ijk}^{(2)}$ corresponds to the direction of the emitted electric field and the second and third to each of the two incoming electric fields of the $\chi^{(2)}$ process. Using these relations, the number of independently contributing $\chi^{(2)}$ elements can oftentimes be reduced considerably as some become zero and some are related to each other.

An immediate consequence of 2.2.12 is that media with inversion symmetry do not facilitate second-order nonlinear effects, i.e. $\chi^{(2)} = 0$ as equation 2.2.12 for the inversion operator I , with $I \cdot \hat{\mathbf{e}} = -\hat{\mathbf{e}}$, yields $\chi_{ijk}^{(2)} = -\chi_{ijk}^{(2)} = 0$ [7].

Furthermore, second harmonic generation shows additional symmetry properties due to its specific geometry. As the two incoming fields have the same frequency, the second and third subscripts of $\chi_{ijk}^{(2)}$ are equivalent, resulting in the general (material-independent) relation $\chi_{ijk}^{(2)} = \chi_{ikj}^{(2)}$ for SHG.

2.3. Properties of Quartz

Quartz is a very common mineral that naturally occurs in the earth's continental crust. It has a chemical formula of SiO_2 and undergoes a phase transition from α -quartz to β -quartz at a temperature of around 846 K [24]. This section provides some details about its crystal structure and physical properties.

2.3.1. Crystal Structure and Symmetry

Crystalline quartz consists of SiO_4 silicon-oxygen tetrahedra where each oxygen atom is shared between two silicon atoms, giving it a net chemical formula of SiO_2 . The crystal structure of α -quartz is depicted in figure 2.3.

At a critical temperature of $T_C = 846$ K, the phase transition from α -quartz to β -quartz takes place. At this transition, atoms in the crystal lattice get slightly displaced relative to each other without changing positions within the lattice. Also, all bonds stay intact. This kind of transition is called a *displacive* transition which happens almost instantaneously. During this transition, the quartz crystal changes from a trigonal crystal structure to a hexagonal one.

2.3.2. Phonon Modes

This section is based on experimental data measured by Gervais et al. [24]. In their work, infrared reflectivity spectra have been measured for seven different temperatures ranging from 295 K to 975 K and fitted with the aid of equation 2.1.16 and the factorized form of the dielectric function (equation 2.1.15) which accounts for multiple phonon resonances in the material. From the fit parameters, phonon frequencies and dampings were extracted. Reflectivity data and fits are shown in figure 2.4. The resulting phonon data for $T = 295$ K are listed in table 2.1.

During the $\alpha \rightarrow \beta$ phase transition of quartz, the A_2 modes labeled $j = 1, 3$ and the E modes labeled $j = 3, 5, 8$ become forbidden in the β -phase due to

2. Theoretical Background

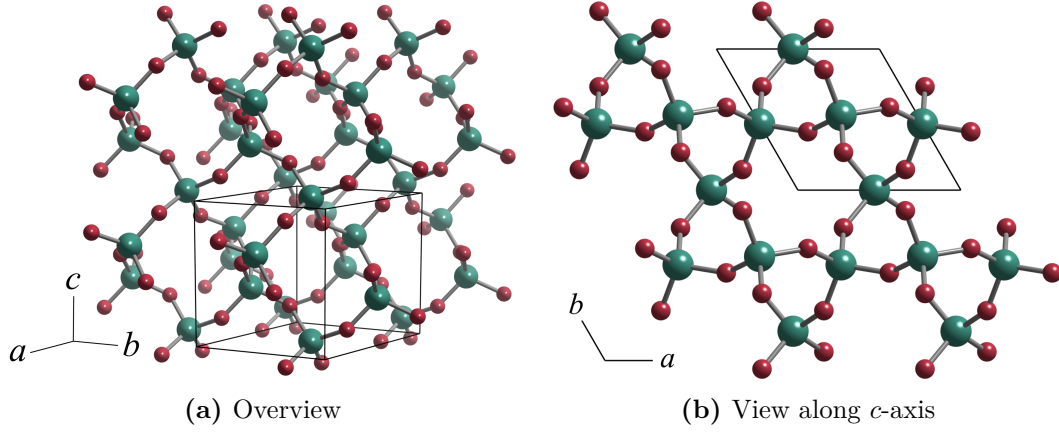


Figure 2.3. Crystal lattice structure of α -quartz (SiO_2) with silicon atoms (green), oxygen atoms (red) and bonds (grey). The black box marks one unit cell. **(a)**: Overview of crystal shape. **(b)**: View along c -axis. Rendered using [25] with data from [26].

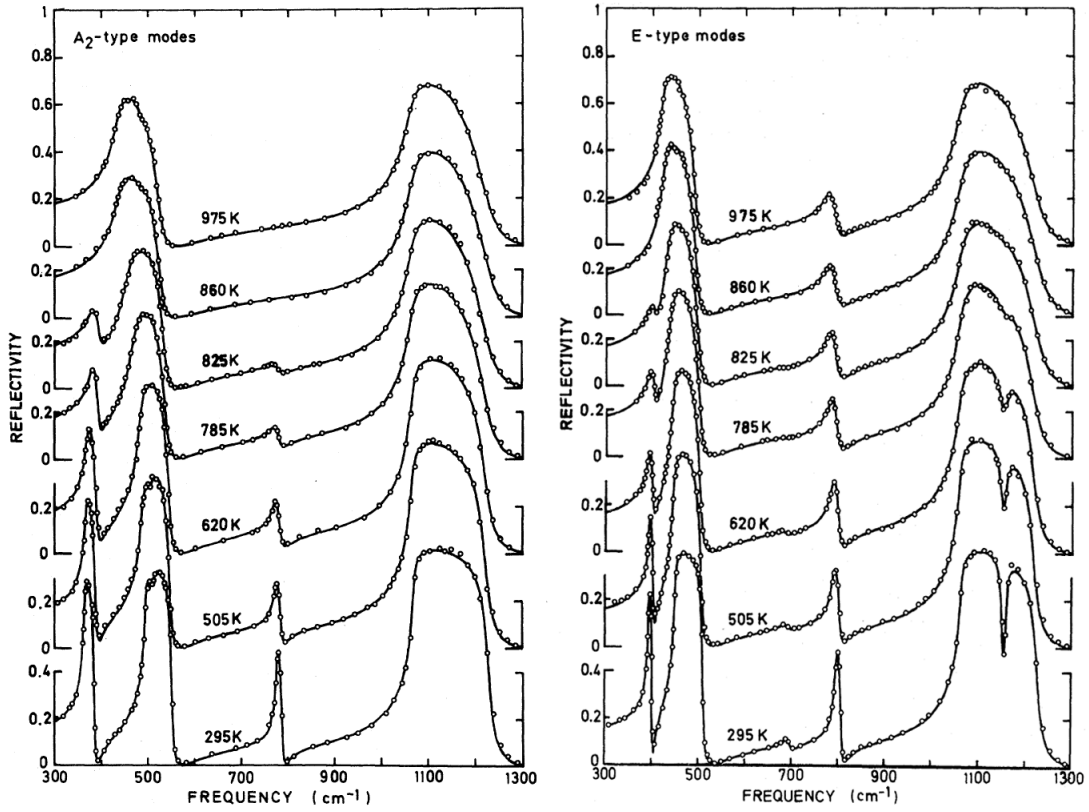


Figure 2.4. Experimental reflectivity data for 7 different temperatures and fits according to equations 2.1.15 and 2.1.16. Taken from reference [24].

Table 2.1. A_2 (extraordinary ray) and E (ordinary ray) phonon modes of α -quartz at room temperature. $\Omega_{j,\text{TO(LO)}}$ denotes the frequency of the j th TO (LO) phonon and $\gamma_{j,\text{TO(LO)}}$ their respective damping. Data taken from reference [24].

A_2 modes					E modes				
j	$\Omega_{j,\text{TO}}$ [cm ⁻¹]	$\Omega_{j,\text{LO}}$ [cm ⁻¹]	$\gamma_{j,\text{TO}}$ [cm ⁻¹]	$\gamma_{j,\text{LO}}$ [cm ⁻¹]	j	$\Omega_{j,\text{TO}}$ [cm ⁻¹]	$\Omega_{j,\text{LO}}$ [cm ⁻¹]	$\gamma_{j,\text{TO}}$ [cm ⁻¹]	$\gamma_{j,\text{LO}}$ [cm ⁻¹]
1	363.5	386.7	4.8	4.8	3	393.5	402	2.8	2.8
2	495	551.5	5.2	5.8	4	450	510	4.5	4.1
3	777	790	6.7	6.7	5	695	697.6	13	13
4	1071	1229	6.8	12	6	797	810	6.9	6.9
$(T = 295 \text{ K})$					7	1065	1226	7.2	12.5
					8	1158	1155	9.3	9.3

structural changes in the crystal [27]. The temperature-dependent phonon data will be used in chapter 3 to simulate spectra of the dielectric function.

With 9 atoms in the primitive cell, α -quartz has 27 phonon branches [28]. Employing symmetry selection rules, leaves 9 phonon branches along the Γ -A direction (along optic axis) and 13 branches along the Γ -K-M direction (perpendicular to optic axis). Phonon dispersion curves of α -quartz have been measured with neutron scattering [28] and are shown in figure 2.5.

2. Theoretical Background

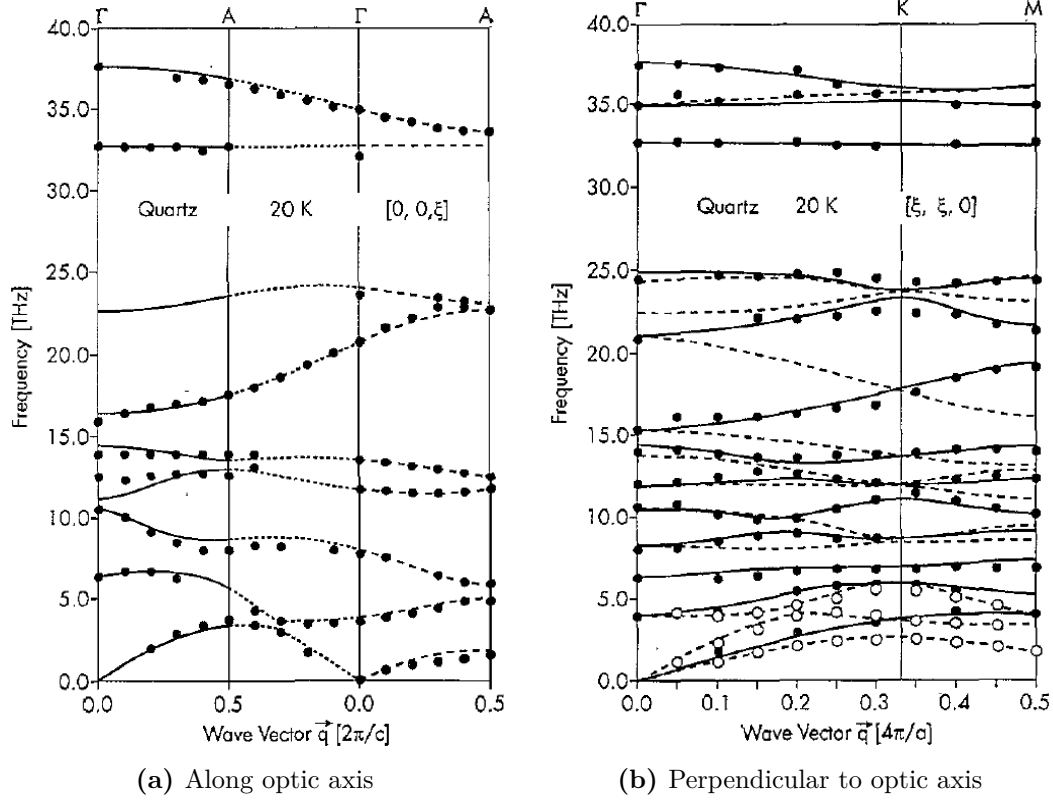


Figure 2.5. Phonon dispersion of α -quartz at $T = 20$ K measured with neutron scattering. (a): Along optic axis and (b): perpendicular to optic axis. Taken from [28].

2.4. Working Principle of Free-Electron Lasers

Unlike conventional lasers which utilize electronic transitions in the lasing material, free-electron lasers generate radiation by transforming the kinetic energy of relativistic electrons into electromagnetic wave energy. Thereto, a relativistic electron beam is injected into a periodic array of permanent magnets (a so-called undulator) which causes emission of synchrotron radiation.

This section sketches the working principle of free-electron lasers, covering a typical setup, relativistically moving electrons and beam creation using undulators in the laser cavity. This section is largely based on Toshiyuki Shiozawa's "*Classical Relativistic Electrodynamics*" [29] and Sándor Varró's "*Free Electron Lasers*" [30].

2.4.1. Basic Setup

The first theoretical treatment of fast moving electrons in a periodic array of permanent magnets was carried out by Motz in 1951 [31] until, in 1977, the first free-electron laser went into operation at Stanford University [32, 33].

The basic setup of a free-electron laser comprises a linear electron accelerator

(linac) capable of achieving relativistic velocities, an array of permanent magnets with alternating polarities (also called an undulator), as well as a lasing cavity confined by a pair of mirrors as shown in figure 2.6.

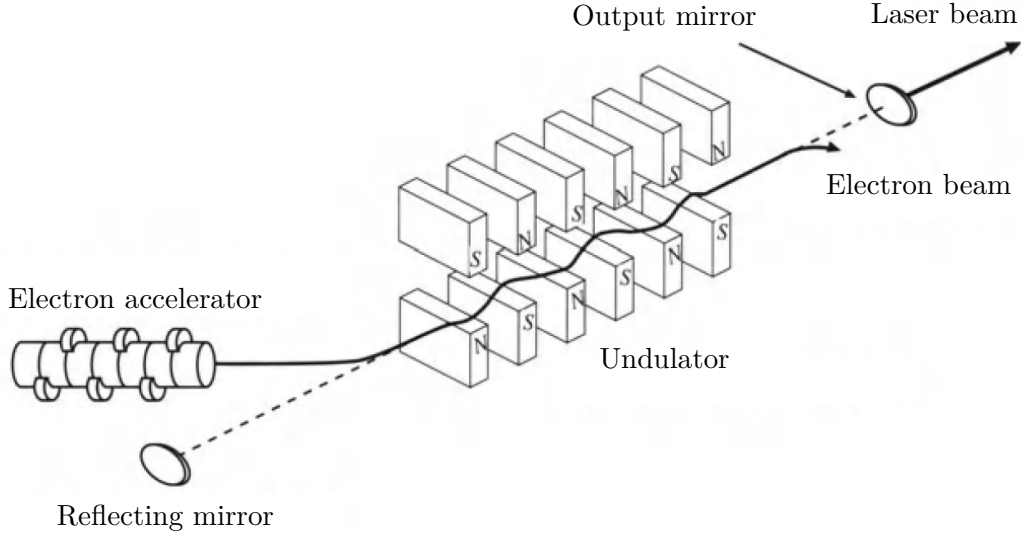


Figure 2.6. Basic setup of a free-electron laser: Relativistic electrons are injected into the undulator using bending magnets where synchrotron radiation is generated. Taken from reference [29].

As an electron enters the undulator along its center axis, it performs a wiggling motion due to the Lorentz force induced by the magnetic field of the undulator's permanent magnets. Every time the electron's orbit is bent, resulting in an accelerated motion, the additional kinetic energy is emitted in the form of synchrotron radiation. This radiation needs to interfere constructively with itself at each corner of the electron's orbit. This condition is further discussed in the forthcoming section. The emitted radiation is then amplified in the cavity and finally ejected through the output mirror.

2.4.2. Synchrotron Radiation in an Undulator

According to special relativity, the total energy E of a particle with mass m and velocity v is given by

$$E = m_0 \gamma c^2 \quad \text{with} \quad \gamma = \frac{1}{\sqrt{1 - \beta^2}} \quad (2.4.1)$$

where $\beta = v/c$ is the reduced velocity and γ is called the relativistic factor. m_0 and c denote, respectively, the particle's rest mass and the speed of light.

The total energy E is the sum of the particle's kinetic energy and its mass energy which is given by $m_0 c^2$. Therefore, γ is a measure of the particle's total energy and $\gamma - 1$ of its kinetic energy. In the high-energy case (i.e. $\gamma \gg 1$), the

2. Theoretical Background

reduced velocity can be expressed as $\beta \simeq 1 - \frac{1}{2\gamma^2}$ (Taylor series up to second order) and the particle is said to be ultra-relativistic.

For free-electron lasers, we consider a beam of electrons with mass m_e and charge e . The electron beam's power P is:

$$P = IE \quad (2.4.2)$$

where I is the current. The power of the electron beam is the free-electron laser's analog to a conventional laser's pump power [30].

A free-electron laser's undulator is usually made of periodically arranged pairs of permanent magnets with alternating polarities, creating a magnetic field B_y along the y -axis of the form (see figure 2.7) [29]:

$$B_y = B_0 \sin\left(\frac{2\pi z}{\lambda_u}\right). \quad (2.4.3)$$

Here, λ_u denotes the spatial period of the permanent magnets (and also of the magnetic field) and B_0 the magnetic field's peak intensity.

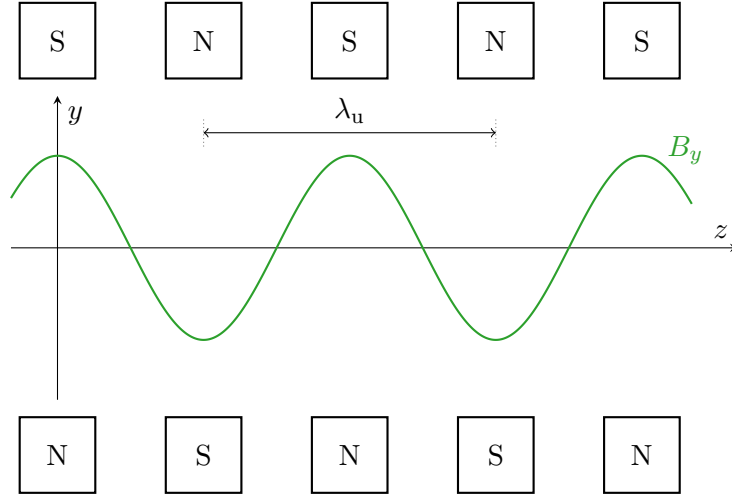


Figure 2.7. Scheme of the center plane of an undulator. The spatial period λ_u is the same for both, the undulator and the magnetic field B_y inside the magnets.

An electron entering the undulator undergoes a Lorentz force-induced wiggling motion along the z -direction perpendicular to and with the same spatial period as the magnetic field. Every time the electron beam is bent at the corners of its orbit, it radiates synchrotron radiation. In order for electromagnetic wave pulses emitted from adjacent corners of the electron's orbit to interfere constructively, the following condition must be met [29]:

$$n\lambda = c \frac{\lambda_u}{\bar{v}_z} - \lambda_u \cos \theta \quad (2.4.4)$$

where λ denotes the optical wavelength of the electromagnetic wave pulses, \bar{v}_z the average velocity of the electron beam along the z -direction and θ the angle

between the z -direction and the direction of pulse propagation (see figure 2.8). n is an integer representing the order of inference, meaning that $n = 1$ stands for the fundamental wavelength and $n > 1$ corresponds to higher harmonics. This whole process can be considered as a kind of spontaneous emission.

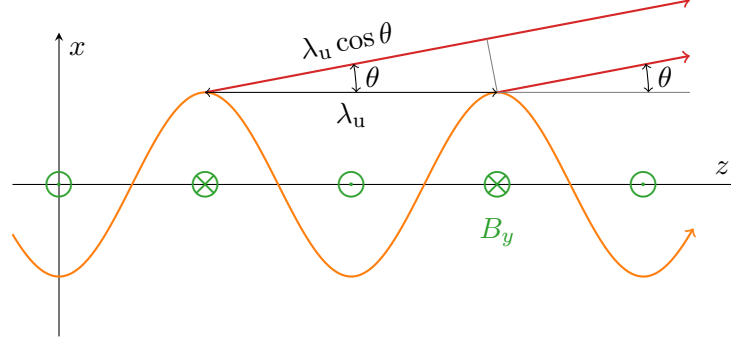


Figure 2.8. An electron's orbit through the center plane of an undulator. For wave pulses to interfere constructively, the phase advance must be a multiple integer of the optical wavelength λ .

2.4.3. Microbunching

In order to get temporally coherent radiation from the light source, there must be a mechanism that corresponds to stimulated emission. In the case of free-electron lasers, this mechanism is given by an interaction of the electrons with the radiation in the lasing cavity. The electromagnetic field generated by the electrons via synchrotron radiation modulates the electron beam spatially such that some electrons lose energy to the optical field and decelerate while some electrons gain energy from the electric field and accelerate, depending on the relative phase of the electrons' transversal velocity to the optical field. These processes correspond to absorption and gain, respectively. This effect is oftentimes referred to as microbunching. If the electron beam is injected at the resonant energy, i.e. at an energy at which the electron slips back exactly one radiation period λ for every undulator period λ_u (see equation 2.4.4), the relative phase between the electrons and the optical field is constant and absorption and gain compensate each other, resulting in zero net gain. To get a positive net gain, the electron beam needs to have an energy slightly above the resonant energy, thus getting a phase shift such that more electrons get decelerated by the optical field, resulting in a positive net gain. This process is illustrated in figure 2.9 [34].

Practically, by varying the electron energy, the lasing regime shifts within the spectrum of the synchrotron radiation, i.e. the emitted optical wavelength λ where lasing takes place, moves such that it reaches the off-resonant case.

2. Theoretical Background

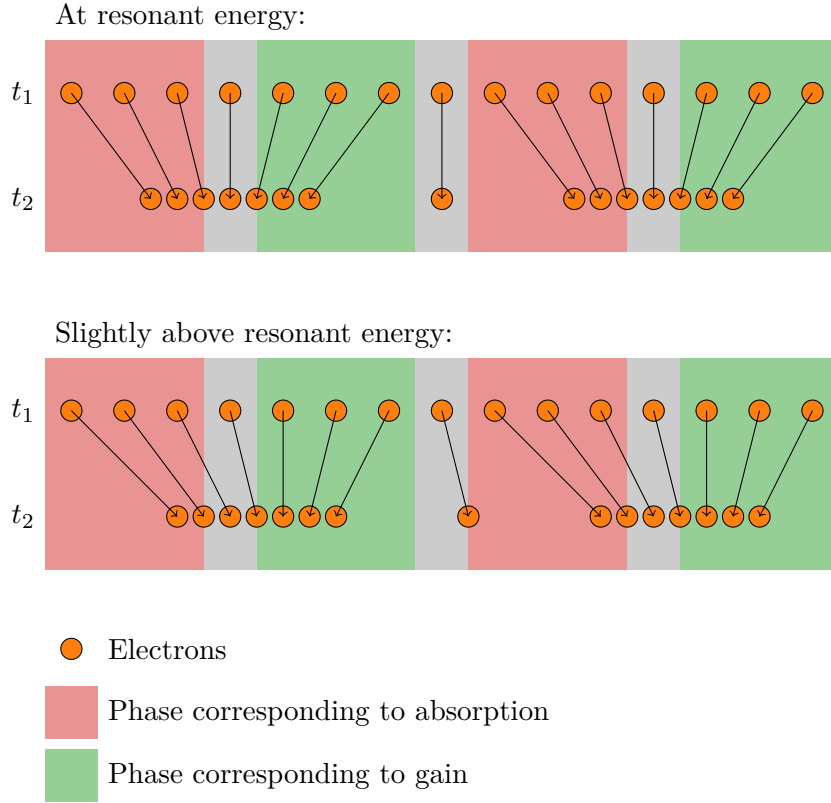


Figure 2.9. A spatially homogeneous electron pulse at time t_1 gets modulated by the optical field. Depending on the relative phase of the electrons' transversal velocity and the optical field, electrons get either accelerated or decelerated which leads to microbunching (time t_2). The resonant case results in zero net gain while an electron energy slightly above resonance leads to a positive net gain which is required for lasing.

2.4.4. Cavity Detuning

Most free-electron lasers allow for a variation of the cavity length L which is defined as:

$$L = L_0 - q\lambda \quad (2.4.5)$$

where L_0 is the nominal cavity length, λ the wavelength of the emitted radiation and q a user-defined value. Keeping q constant over a wavelength scan increases the accessible spectral range and maintains the relative bandwidth of the free-electron laser [4]. By varying the cavity detuning $\Delta L = q\lambda$, the spectral bandwidth can be adjusted and therefore the achievable pulse duration as bandwidth and pulse duration are related by the time-bandwidth product.

For nonlinear spectroscopy, short pulses are advantageous as they yield higher peak intensities and thus more generated nonlinear signal. However, this gain in nonlinear signal comes at the cost of spectral resolution as the spectral bandwidth of the emitted pulses increases.

3. Simulations

3.1. Dispersion of the Dielectric Function

Good knowledge of the dielectric function is necessary to calculate Fresnel coefficients which affect both SHG and reflectivity spectra. Temperature-dependent phonon data for quartz from Gervais et al. [24] have been used to parametrize frequency shifts and changes in the dampings as the temperature varies. A quadratic polynomial fit has been applied to the temperature-dependent data to interpolate values for $\Omega(T)$ and $\gamma(T)$. From these temperature-dependent phonon data, the dielectric function can be simulated with the aid of equation 2.1.15. Corresponding spectra are shown in figure 3.1 for four different temperatures ranging from 300 K to 840 K.

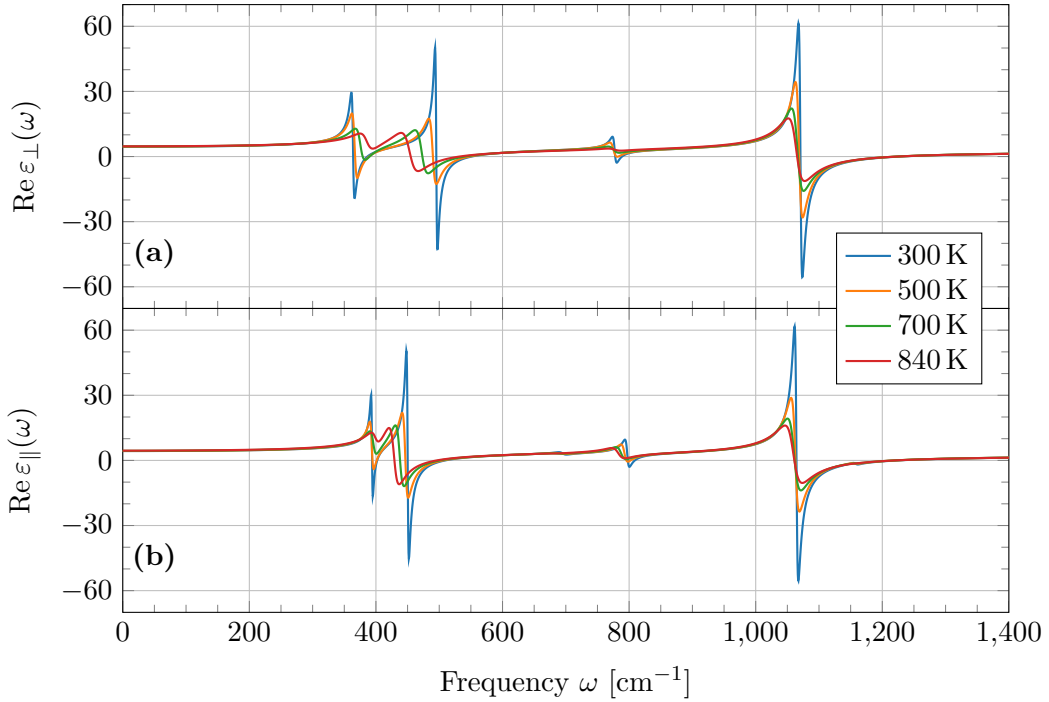


Figure 3.1. Simulated spectra of the real part of the dielectric function for four different temperatures. **(a):** $\epsilon_{\perp}(\omega)$ for extraordinary rays was calculated from A_2 modes and **(b):** $\epsilon_{\parallel}(\omega)$ for ordinary rays from E modes.

3.2. Reflectivity Spectra

Using the Fresnel coefficients of reflectivity (equation 2.1.28) as well as phonon data from Gervais et al. [24] with their corresponding spectra of the dielectric function (see section 3.1), it is possible to calculate the reflected field strengths and thus the intensities of the reflected beam which are given by:

$$I_{r,P} = |E_{r,x}|^2 + |E_{r,z}|^2 = |R_{xx}E_{i,x}|^2 + |R_{zz}E_{i,z}|^2 \quad (3.2.1)$$

and $I_{r,S} = |E_{r,y}|^2 = |R_{yy}E_{i,y}|^2$

for P- and S-polarization, respectively. The calculated spectra are shown in figure 3.2 for four different temperatures (300 K to 840 K) at a constant angle of incidence $\alpha_i = 60^\circ$. Figures 3.3a and 3.3b show calculated reflectivity spectra for four different angles (0° , 30° , 60° , 80°) at a constant temperature $T = 300$ K for P- and S-polarization, respectively. Additionally, the quantities $\text{Im} \varepsilon(\omega)$ and $\text{Im} [-1/\varepsilon(\omega)]$ are plotted in figures 3.3c and 3.3d which peak at TO and LO frequencies, respectively.

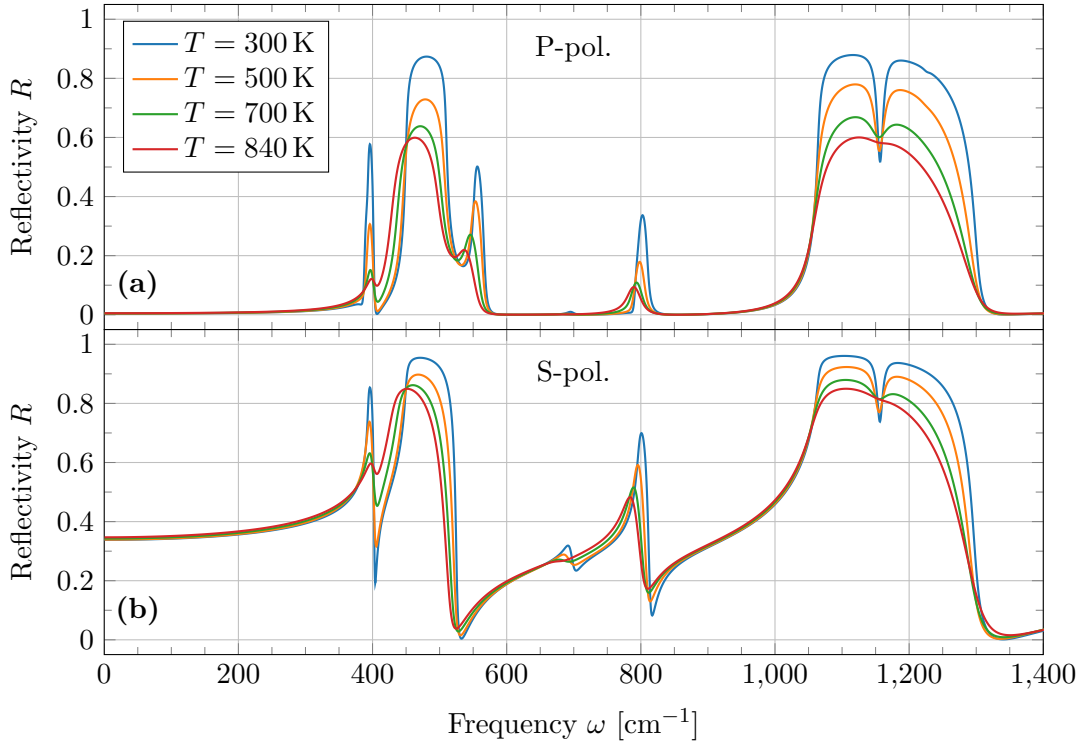


Figure 3.2. Reflectivity spectra for four different temperatures in (a): P- and (b): S-polarization at a constant angle of incidence $\alpha_i = 60^\circ$. Based on data from [24] which were interpolated to extract the temperature dependence.

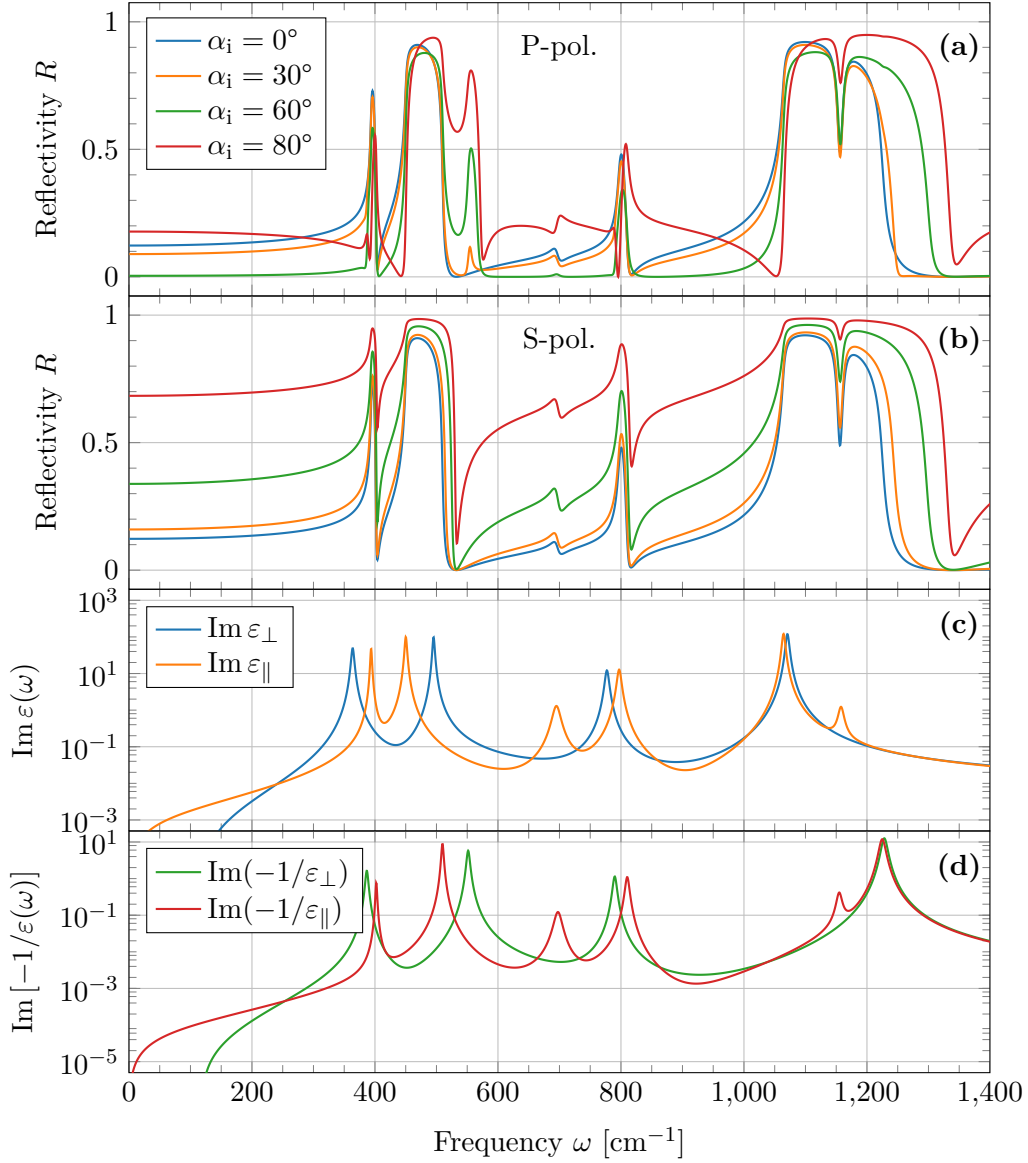


Figure 3.3. (a) and (b): Simulated spectra of the Fresnel-corrected reflectivity R for, respectively, P- and S-polarization at room temperature. (c) and (d): Quantities $\text{Im } \varepsilon(\omega)$ and $\text{Im} [-1/\varepsilon(\omega)]$ serve as reference for TO and LO phonon frequencies, respectively (semi-logarithmic scale). Calculations based on data from [24].

3.3. Azimuthal SHG

Quartz's crystal structure belongs to the trigonal 32 symmetry class (threefold symmetry D_3 about the c -axis, twofold symmetry D_2 about the a -axis). This, according to calculations using equation 2.2.12, results in the following four

3. Simulations

independent non-vanishing elements of the $\chi^{(2)}$ tensor [7]:

$$\begin{aligned}\chi_{aaa}^{(2)} &= -\chi_{abb}^{(2)} = -\chi_{bba}^{(2)} = -\chi_{bab}^{(2)}, \\ \chi_{abc}^{(2)} &= -\chi_{bac}^{(2)}, \\ \chi_{acb}^{(2)} &= -\chi_{bca}^{(2)}, \\ \chi_{cab}^{(2)} &= -\chi_{cba}^{(2)}\end{aligned}\tag{3.3.1}$$

where (a, b, c) gives the set of principle axes with c and a parallel to the threefold and twofold axes, respectively [5].

Additionally, we can invoke specific symmetry considerations for SHG as discussed in section 2.2.2 to considerably reduce the number of contributing $\chi^{(2)}$ elements as the second and third indices are equivalent, meaning that $\chi_{abc} = \chi_{acb}$ and $\chi_{cab} = \chi_{cba} = 0$, leading to χ_{aaa} and χ_{acb} being the only independently contributing elements:

$$\begin{aligned}\chi_{aaa}^{(2)} &= -\chi_{abb}^{(2)} = -\chi_{bba}^{(2)} = -\chi_{bab}^{(2)}, \\ \chi_{abc}^{(2)} &= -\chi_{bac}^{(2)} = \chi_{acb}^{(2)} = -\chi_{bca}^{(2)}.\end{aligned}\tag{3.3.2}$$

The following considerations assume a non-collinear SHG configuration in reflection as depicted in figure 3.4. The second harmonic beam is generated at a frequency $\omega_{\text{SH}} = 2\omega$ along the phase-matched direction which is given by $\mathbf{k}_{\text{SH}}^r = \mathbf{k}_1^r + \mathbf{k}_2^r$. This leads to an angle of reflection $\alpha_{\text{SH}}^r = (\alpha_1^i + \alpha_2^i)/2$.

Starting from equation 2.2.3, the second-order nonlinear polarization in the crystal is given by:

$$\mathbf{P}_{\text{SH}}(2\omega) \propto \chi^{(2)}(\omega) : \left[L_1(\omega) \mathbf{E}_1^i(\omega) \right] \left[L_2(\omega) \mathbf{E}_2^i(\omega) \right]\tag{3.3.3}$$

where $\mathbf{E}_{1(2)}^i(\omega)$ is the first (second) incoming beam and $L_{1(2)}(\omega)$ its respective Fresnel transmission coefficient which is given by equations 2.1.24 and 2.1.27.

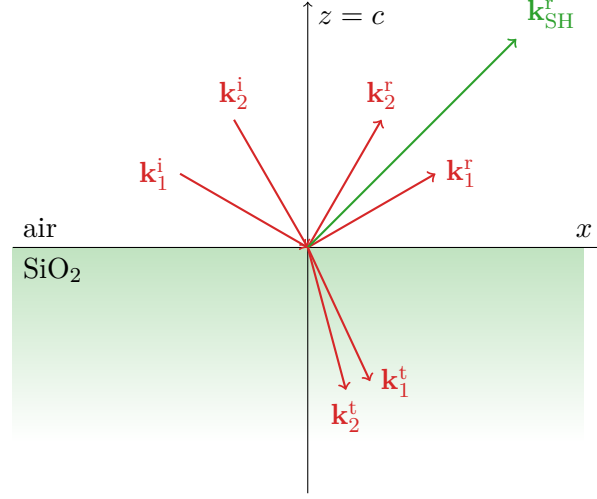


Figure 3.4. Schematic of the non-collinear second harmonic generation in reflection. x - z is chosen as the plane of incidence. The reflected fundamental beams are geometrically separated from the generated second harmonic beam.

The transformation of the $\chi^{(2)}$ elements from the crystal coordinates (a, b, c) to the lab frame (x, y, z) is generally given by [5]:

$$\chi_{ijk}^{(2)} = \sum_{lmn} \chi_{lmn}^{(2)} (\hat{\mathbf{i}} \cdot \hat{\mathbf{l}}) (\hat{\mathbf{j}} \cdot \hat{\mathbf{m}}) (\hat{\mathbf{k}} \cdot \hat{\mathbf{n}}). \quad (3.3.4)$$

Assuming the sample's optic axis along the z -direction and its a -axis at an angle ϕ away from the xz -plane, the coordinate transformation takes the form:

$$\begin{aligned} \hat{\mathbf{a}} &= \hat{\mathbf{x}} \cos \phi + \hat{\mathbf{y}} \sin \phi \\ \hat{\mathbf{b}} &= -\hat{\mathbf{x}} \sin \phi + \hat{\mathbf{y}} \cos \phi \\ \hat{\mathbf{c}} &= \hat{\mathbf{z}}. \end{aligned} \quad (3.3.5)$$

which simply is a rotation about the z -axis. This, together with the contributing $\chi^{(2)}$ elements of equation 3.3.2, results in the following $\chi^{(2)}$ elements in laboratory coordinates:

$$\begin{aligned} \chi_{xxx}^{(2)} &= -\chi_{xyy}^{(2)} = -\chi_{yxy}^{(2)} = -\chi_{yyx}^{(2)} = \chi_{aaa}^{(2)} \cos(3\phi) \\ \chi_{xxy}^{(2)} &= \chi_{xyx}^{(2)} = \chi_{yxx}^{(2)} = -\chi_{yyy}^{(2)} = \chi_{aaa}^{(2)} \sin(3\phi) \\ \chi_{xyz}^{(2)} &= -\chi_{yxz}^{(2)} = \chi_{xzy}^{(2)} = -\chi_{yzx}^{(2)} = \chi_{acb}^{(2)}. \end{aligned} \quad (3.3.6)$$

From these expressions, the azimuthal dependence of the SH signal is already apparent. Furthermore, every possible polarization configuration yields SHG signal. The intensity of the reflected second harmonic beam arises from projecting the second-order nonlinear polarization onto the direction of the reflected electric field. Summing over all possible $\chi^{(2)}$ components for each polarization configuration gives the following components of the reflected SHG signal:

3. Simulations

$$\begin{aligned}
I_{\text{PPP}}^{\text{SHG}} &= \left| (L_{xx} E_{1,x}^i)(L_{xx} E_{2,x}^i) \chi_{aaa}^{(2)} \cos(3\phi) \right|^2 / \Delta k^2, \\
I_{\text{SPP}}^{\text{SHG}} &= \left| \left[(L_{zz} E_{1,z}^i)(L_{xx} E_{2,x}^i) + (L_{xx} E_{1,x}^i)(L_{zz} E_{2,z}^i) \right] \chi_{acb}^{(2)} \cdots \right. \\
&\quad \left. \cdots + (L_{xx} E_{1,x}^i)(L_{xx} E_{2,x}^i) \chi_{aaa}^{(2)} \sin(3\phi) \right|^2 / \Delta k^2, \\
I_{\text{PSS}}^{\text{SHG}} &= \left| (L_{yy} E_{1,y}^i)(L_{yy} E_{2,y}^i) \chi_{aaa}^{(2)} \cos(3\phi) \right|^2 / \Delta k^2, \\
I_{\text{SSS}}^{\text{SHG}} &= \left| (L_{yy} E_{1,y}^i)(L_{yy} E_{2,y}^i) \chi_{aaa}^{(2)} \sin(3\phi) \right|^2 / \Delta k^2, \\
I_{\text{PSP}}^{\text{SHG}} &= \left| (L_{yy} E_{1,y}^i)(L_{zz} E_{2,z}^i) \chi_{acb}^{(2)} - (L_{yy} E_{1,y}^i)(L_{xx} E_{2,x}^i) \chi_{aaa}^{(2)} \sin(3\phi) \right|^2 / \Delta k^2, \\
I_{\text{SSP}}^{\text{SHG}} &= \left| (L_{yy} E_{1,y}^i)(L_{xx} E_{2,x}^i) \chi_{aaa}^{(2)} \cos(3\phi) \right|^2 / \Delta k^2
\end{aligned} \tag{3.3.7}$$

where $\Delta k = |\mathbf{k}_{\text{SH}}^t - \mathbf{k}_1^t - \mathbf{k}_2^t|$ is the wave vector mismatch which accounts for reflective phase matching and can be calculated using equations 2.1.21 and 2.1.25 and $I_{\text{LMN}}^{\text{SHG}}$ denotes the SHG intensity for M- and N-polarized incoming beams and L-polarized SH output. As the z component of the reflected SHG signal is zero for all polarization configurations, the P- and S-polarized output can be directly read out from the x and y components, respectively. Figure 3.5 gives plots according to the model described in equation 3.3.7 for three different ratios $\chi_{aaa}^{(2)} / \chi_{acb}^{(2)}$ when setting Fresnel coefficients L_{kk} and electric fields E_k to 1.

3.3.1. Surface Contribution

These symmetry considerations are only valid in the bulk of the crystal and are broken at the surface. There, the crystal has different symmetry properties and hence belongs to a different symmetry group with different independent non-vanishing $\chi^{(2)}$ elements which for the surface of an α -quartz c -cut, is the hexagonal 6mm symmetry class (sixfold symmetry C_{6v}) with elements [7, 6]:

$$\begin{aligned}
\chi_{\text{S},aac}^{(2)} &= \chi_{\text{S},bbc}^{(2)}, \\
\chi_{\text{S},aca}^{(2)} &= \chi_{\text{S},bcb}^{(2)} \approx \chi_{\text{S},caa}^{(2)} = \chi_{\text{S},cbb}^{(2)}, \\
\chi_{\text{S},ccc}^{(2)} &
\end{aligned} \tag{3.3.8}$$

where the subscript S denotes the surface contribution. The resulting surface SHG, if detectable, is expected to yield no azimuthal dependence due to the hexagonal crystal symmetry at the surface.

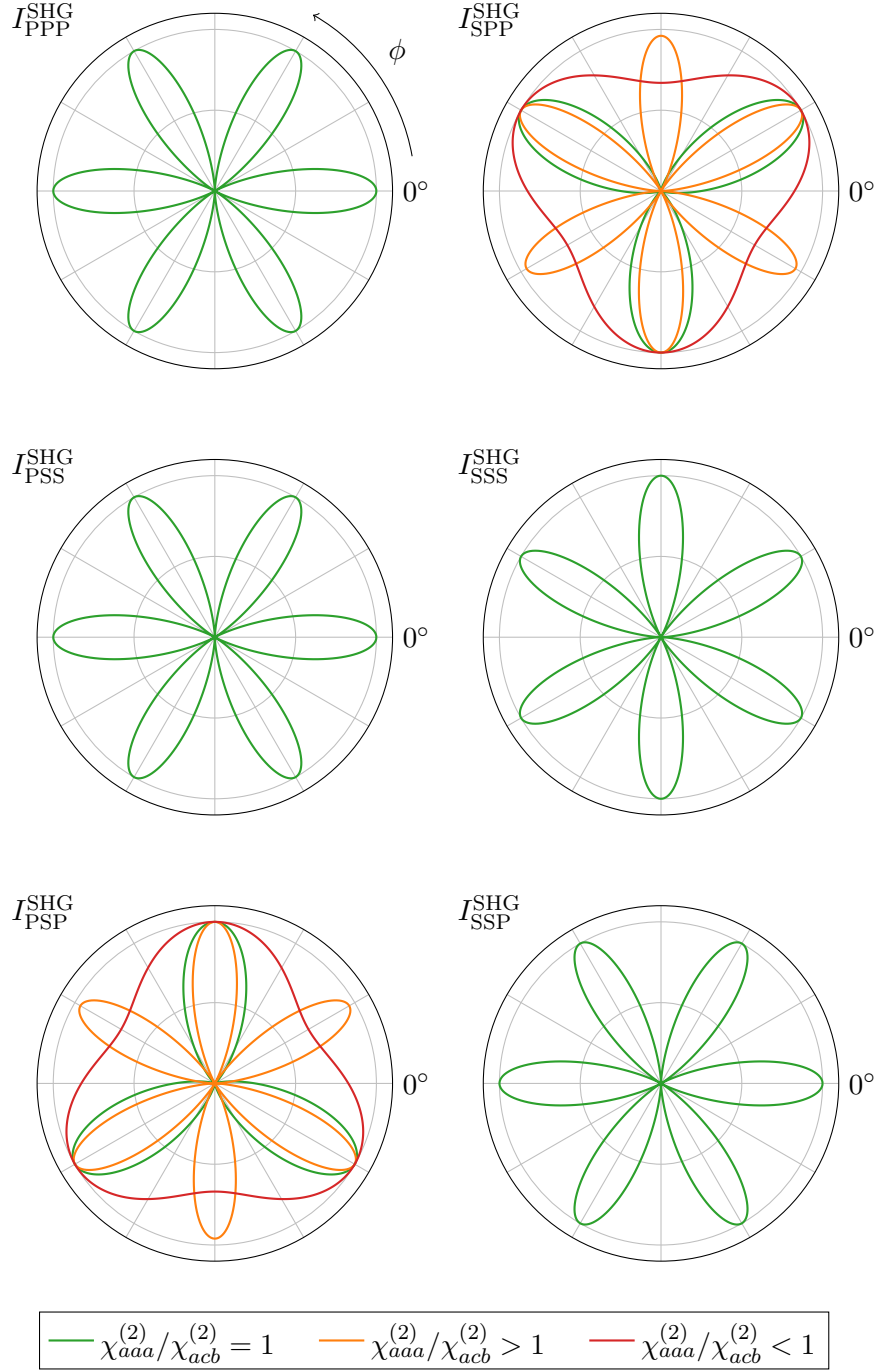


Figure 3.5. Plots of the calculated azimuthal intensity model according to equation 3.3.7 for the three cases $\chi_{aaa}^{(2)} = \chi_{acb}^{(2)}$, $\chi_{aaa}^{(2)} > \chi_{acb}^{(2)}$ and $\chi_{aaa}^{(2)} < \chi_{acb}^{(2)}$ where $\chi_{acb}^{(2)}$ only contributes to I_{SPP}^{SHG} and I_{PSP}^{SHG} . Fresnel coefficients and electric field are set to $L_{kk} = E_k = 1$.

3. Simulations

3.3.2. β -Quartz

At a transition temperature of $T_C = 573^\circ\text{C}$, α -quartz undergoes the phase transition to β -quartz, also known as high quartz. This phase transition comes with a change in crystal symmetry, namely from the trigonal 32 to the hexagonal 622 symmetry class (D_6 Schoenflies) [35, 36]. As a result, the contributing $\chi^{(2)}$ elements change accordingly to the following [7]:

$$\begin{aligned}\chi_{\beta,abc}^{(2)} &= -\chi_{\beta,bac}^{(2)} = \chi_{\beta,acb}^{(2)}, \\ \chi_{\beta,cab}^{(2)} &= -\chi_{\beta,cba}^{(2)}.\end{aligned}\tag{3.3.9}$$

As before, applying SHG-specific symmetry rules yields a considerable reduction of the contributing $\chi^{(2)}$ tensor elements to just one unique contribution for β -quartz which is the first line of equation 3.3.9. Carrying out the coordinate transformation from the crystal frame into the lab frame as described above yields that solely the following two polarization components yield SHG signal:

$$\begin{aligned}I_{\text{SPP}}^{\text{SHG}} &= \left| \left[(L_{zz}E_{1,z}^i)(L_{xx}E_{2,x}^i) + (L_{xx}E_{1,x}^i)(L_{zz}E_{2,z}^i) \right] \chi_{\beta,acb}^{(2)} \right|^2 / \Delta k^2, \\ I_{\text{PSP}}^{\text{SHG}} &= \left| (L_{yy}E_{1,y}^i)(L_{zz}E_{2,z}^i) \chi_{\beta,acb}^{(2)} \right|^2 / \Delta k^2.\end{aligned}\tag{3.3.10}$$

These results imply that for β -quartz no azimuthal dependence is expected while SPP and PSP polarizations still yield a constant contribution proportional to $\chi_{\beta,acb}^{(2)}$.

4. Experimental Setup

This chapter lays out the experimental details on the measurements that have been conducted within the scope of this work. This includes technical information on the light source, i.e. the free-electron laser of the Fritz Haber Institute in Berlin (FHI FEL), the autocorrelation setup used to produce and detect SHG signals in the sample as well as a beamline width characterization of the whole setup to estimate spot sizes in the focus.

4.1. The FHI Free-Electron Laser

The FHI FEL was installed in 2011 in a dedicated building at the FHI campus in Berlin and put into operation in November 2013 [4].

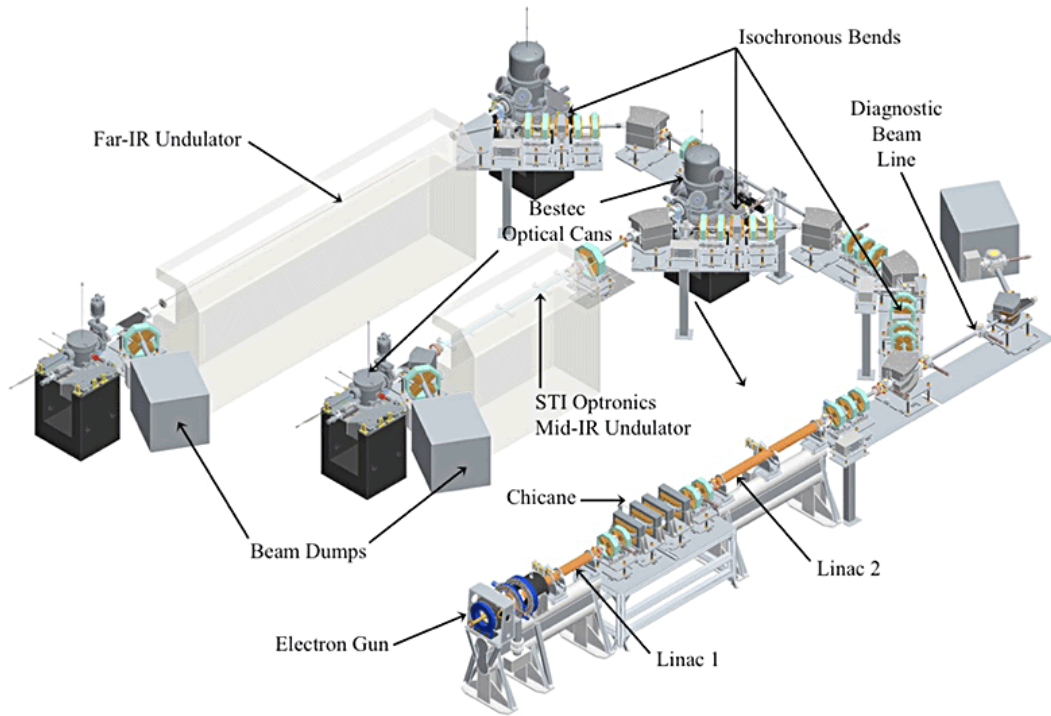


Figure 4.1. Setup of the FHI FEL. Two linear accelerators (Linac 1 and 2) induce electron energies of 15 MeV to 50 MeV. Afterwards, the electron beam is guided to one of two undulators where infrared laser radiation is generated. Taken from [4].

The general setup is shown in figure 4.1. It comprises a thermionic gridded electron gun and two linear accelerators (linacs) of which the first accelerates

4. Experimental Setup

to a nominal electron energy of 20 MeV and the second accelerates or decelerates to a final electron energy of 15 MeV to 50 MeV. Afterward, the electron beam is bent by 90° isochronous achromats into the MIR undulator which has a period length $\lambda_u = 40$ mm with 50 periods and an overall length of 2 m. The minimal undulator gap is 16.5 mm [4]. The lasing cavity is confined by two spherical concave gold-plated copper mirrors with radii of curvature of 2.65 m and 3.51 m, respectively, resulting in a Rayleigh length of the cavity mode of 2 m which corresponds to the undulator length. There are 5 outcoupling mirrors available with outcoupling holes of diameters 0.75 mm, 1.0 mm, 1.5 mm, 2.5 mm and 3.5 mm. The most important specifications of the setup are summarized in table 4.1.

Future plans of extending the setup by a second undulator to reach longer wavelengths in the far-infrared (FIR) involve a second beam line which would allow to cover the wavelength region from 40 μm to 500 μm .

Table 4.1. Specifications of the FHI FEL electron beamline in the mid-infrared spectral region. Data taken from [4].

Parameter	Value
Undulator period	40 mm
Number of periods	50
Undulator length	2.0 m
Cavity length	5.4 m
Electron energy	15 MeV to 50 MeV
Wavelength range	4 μm to 48 μm
Micropulse length	1 ps to 5 ps
Micropulse repetition rate	1 GHz
Macropulse length	1 μs to 15 μs
Macropulse Repetition rate	5 Hz to 10 Hz

4.1.1. Pulse Structure

The time structure of the FHI FEL is composed of macro-pulses of which each again has a pulsed substructure of a few thousand micro-pulses.

The electron gun is driven at a repetition rate of 1 GHz which corresponds to the micro-pulse repetition rate. Those micro-pulses then enter a 1 GHz buncher to reduce the bunch length, resulting in a micro-pulse length of 1 ps to 5 ps. This is necessary for the linacs to be able to effectively capture and accelerate the electrons. The linacs then introduce a macro-pulsed structure with macro-pulse lengths of 1 μs to 15 μs at a repetition rate of 5 Hz to 10 Hz. The pulse structure is shown in figure 4.2.

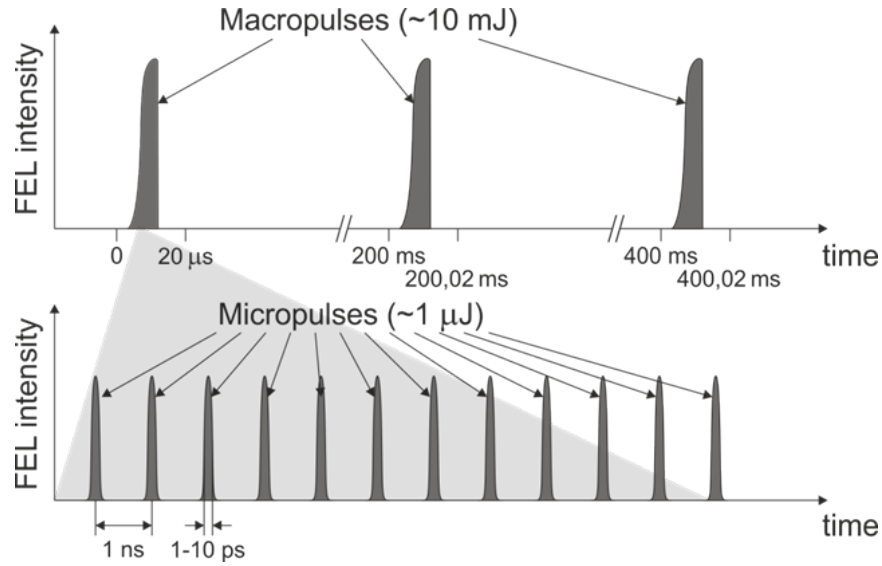


Figure 4.2. Pulse structure of the FHI FEL. Macro-pulses at a repetition rate of 5 Hz to 10 Hz have a subpulse structure comprising micro-pulses at a repetition rate of 1 GHz. Taken from [4].

4.2. The SHG Setup

The experimental setup mainly resembles a common non-collinear autocorrelator comprising a beam splitter, two excitation arms and one linear translation stage to adjust for time zero. The basic setup is shown in figure 4.3.

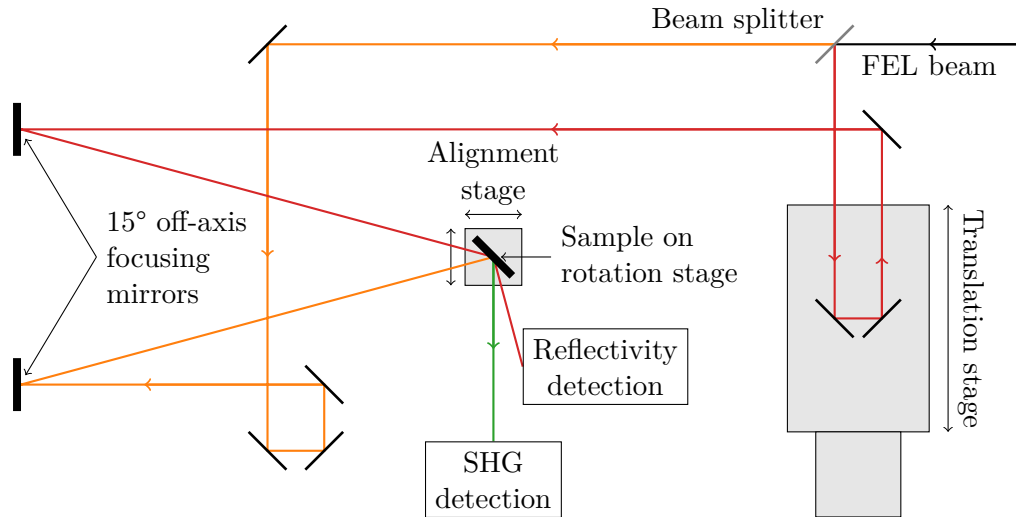


Figure 4.3. Schematic of the SHG autocorrelator setup. The collimated FEL beam (black line) is split into the excitation arms (yellow and red lines) and focused onto the sample. The generated SH signal (green line) is then detected using an MCT/InSb sandwich detector and the reflected FEL beam (red) with a pyroelectric sensor.

4. Experimental Setup

First, the collimated FEL beam is geometrically split into its upper and lower half using a rectangular gold mirror with a sharp edge which ensures wavelength-independent splitting over the entire IR spectral region. One excitation beam is led over a motorized linear translation stage to shift its beam path relative to the other excitation beam to achieve temporal overlap of the FEL pulses on the sample. Both excitation beams are then focused onto the sample using 15° off-axis focusing gold mirrors ($f = 517$ mm). Long focal lengths compared to a previously existing setup were deliberately chosen to achieve large spot sizes in the focus. Experience in a previous setup showed that the FEL power needed to be attenuated to approximately 10% in order to not exceed the damage threshold of the quartz sample. Larger spot sizes allow for more power of the exciting laser and therefore more signal while keeping the photon fluence below a critical value at which sample damage occurs.

The sample is mounted on a motorized 360° rotation stage (Newport) which facilitates azimuthal scans around the sample's surface normal.

Generally, only gold-plated reflecting optics have been used in the setup to guarantee largely wavelength-independent beam control. Also, a variety of IR windows and edgepass filters have been used to either suppress intrinsic harmonics of the FEL that would otherwise produce light scatter, or to block the FEL's fundamental wavelengths in front of the SHG detection to obtain solely the generated SH signal. These filtering optics include $7\text{ }\mu\text{m}$ longpass/shortpass filters, $9\text{ }\mu\text{m}$ and $13.5\text{ }\mu\text{m}$ longpass filters (LOT) as well as magnesium fluoride (MgF_2), calcium fluoride (CaF_2), zinc sulphide (ZnS) and zinc selenide (ZnSe) windows (Korth) serving as $6\text{ }\mu\text{m}$, $8\text{ }\mu\text{m}$, $13.8\text{ }\mu\text{m}$ and $20.5\text{ }\mu\text{m}$ shortpass filters, respectively.

For polarization-dependent measurements, wire grid polarizers (Thorlabs) have been used which absorb IR radiation polarized parallel to the wires' orientation and transmit the perpendicular component. Initially, the incoming FEL beam is P-polarized. Using two polarizers sequentially, one at a 45° orientation, the second in S-transmittance, the incoming polarization of the FEL can be rotated to S-polarization. The resulting transmitted power is about 10% of the incoming power. With one additional polarization filter (three in total), all polarization configurations can be achieved for the two excitation arms and the detection.

4.2.1. Detection

The sample is mounted at an angle of 45° , resulting in an angle of incidence $\alpha_i = 60^\circ$ for the more grazing reflected beam. The SHG signal emerges between both reflected beams and gets recollimated using a 90° off-axis focusing gold mirror ($f = 191$ mm) and finally refocused ($f = 102$ mm) onto a nitrogen-cooled MCT/InSb (mercury cadmium telluride/indium antimonide) semiconductor sandwich detector (InfraRed Associates, Inc.). The non-collinear setup allows for background-free detection as the reflected beams are spatially separated from the generated SH signal. The reflected beam is recollimated

and focused onto a pyroelectric detector using a concave spherical gold mirror ($f = 100$ mm).

In order to compensate for power drifts of the FEL, a small portion (approximately 5%) of the incoming FEL beam is split onto another pyroelectric detector using a potassium bromide (KBr) window as a beam splitter for power reference. All signals are recorded and digitized with a GHz oscilloscope (Teledyne LeCroy) and processed using a LabVIEW routine.

4.2.2. Samples and Probe Heater

For measurements at room temperature, a crystalline α -quartz window (Korth) with a diameter of 45 mm and a thickness of 3 mm has been mounted on the rotation stage. The sample's surface is cut perpendicularly to the optic crystal axis (c -cut) and optically polished.

For temperature-dependent measurements, smaller α -quartz windows (diameter: 8 mm, thickness: 1 mm, Crystal GmbH) have been used to facilitate the use of a probe heater which is depicted in figure 4.4. The heating voltage has been adjusted by a controller (Eurotherm) to keep the sample constantly at the set temperature. Feeler gauges inside the heater's body served as feedback for the controller.

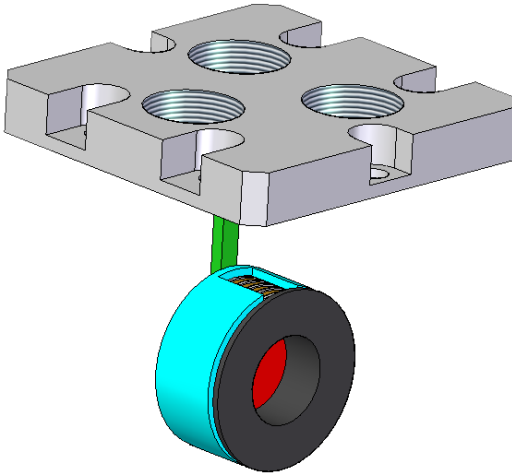


Figure 4.4 Schematic of the probe heater. A heating wire inside the cover (blue) surrounds the heater's body (black) which is in contact with the quartz sample (red).

4.3. Beamline Characterization

Doing calculations according to Gaussian beam optics as discussed in appendix A allows an estimation of the beamline in the real experiment. Particularly interesting for the alignment of the sample are the focus position, the beam width in the focus and the Rayleigh length as well as their behavior as a function of the wavelength. Knowing the parameters of the used optical elements, the beamline can be theoretically retraced by applying the ABCD law of Gaussian beam optics (cf. section A.3). A beam line simulation for the SHG setup was

4. Experimental Setup

done using a LabVIEW application written and provided by courtesy of Frans Wijnen, Radboud University Nijmegen, Netherlands, and is shown in figure 4.5 for four relevant wavelengths. Spot sizes on the sample and Rayleigh lengths for these wavelengths are given in table 4.2.

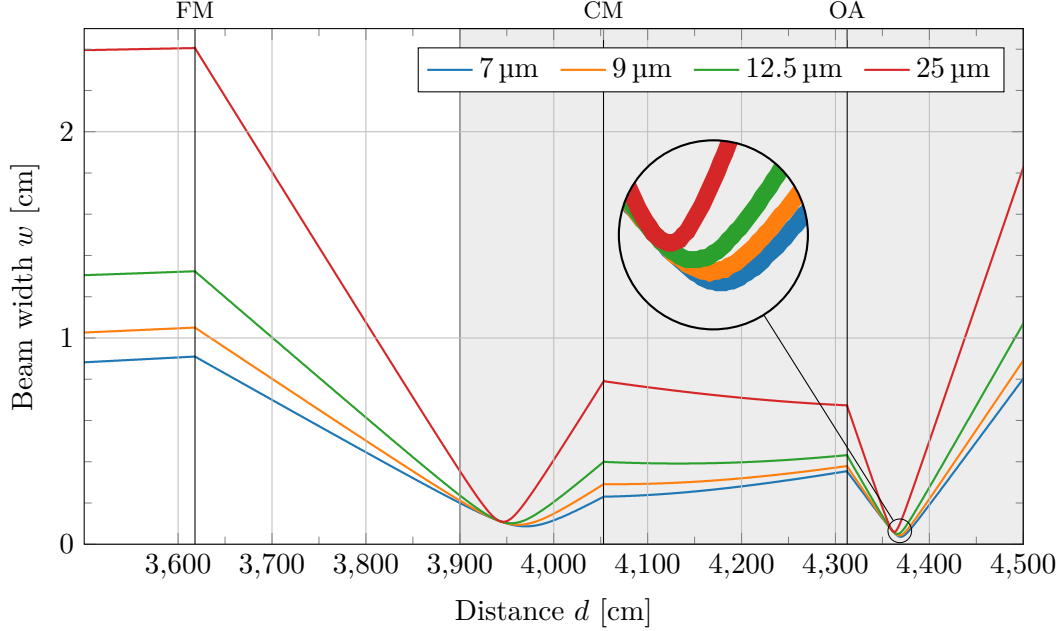


Figure 4.5. Beamline simulation for the SHG experiment. The FEL beam is focused onto the optic table (grey shade) with a 90° off-axis focusing mirror (FM) and collimated using a concave focusing mirror (CM). After being split, both excitation arms are focused onto the sample with 15° off-axis focusing mirrors (OA). Distance d is measured with respect to the diagnostic chamber behind the outcoupling mirror of the FEL.

Table 4.2 Spot sizes w_0 on the sample and Rayleigh lengths z_R for the four plotted wavelengths in figure 4.5.

λ [μm]	ω [cm^{-1}]	w_0 [mm]	z_R [mm]
25	400	0.6	14.85
12.5	800	0.5	25.91
9	1111	0.42	31.06
7	1429	0.36	33.69

Additionally, using an infrared camera, the beam profiles of the two incoming beams were measured at $\omega = 800 \text{ cm}^{-1}$. For that, the camera was placed slightly behind the position of spatial overlap of the two foci to see both excitation beams. A picture of the beam profiles is given in figure 4.6. The measured intensities were integrated along the x - and the z -axes (also shown in figure 4.6). Fitting the z -integrated intensities with Gaussian functions

$$f(x) = ae^{-\frac{(z-b)^2}{2c^2}} \quad (4.3.1)$$

allows for determination of the respective beam widths. Fit parameters are given in table 4.3. From these fit parameters, the beam widths (defined as in section A.2) can be calculated ($w = \sqrt{2}c$) to be $w_1 = (0.62 \pm 0.03)$ mm and $w_2 = (0.59 \pm 0.04)$ mm for left and right beam, respectively, which is in satisfactory agreement with the simulation ($w_0 = 0.5$ mm).

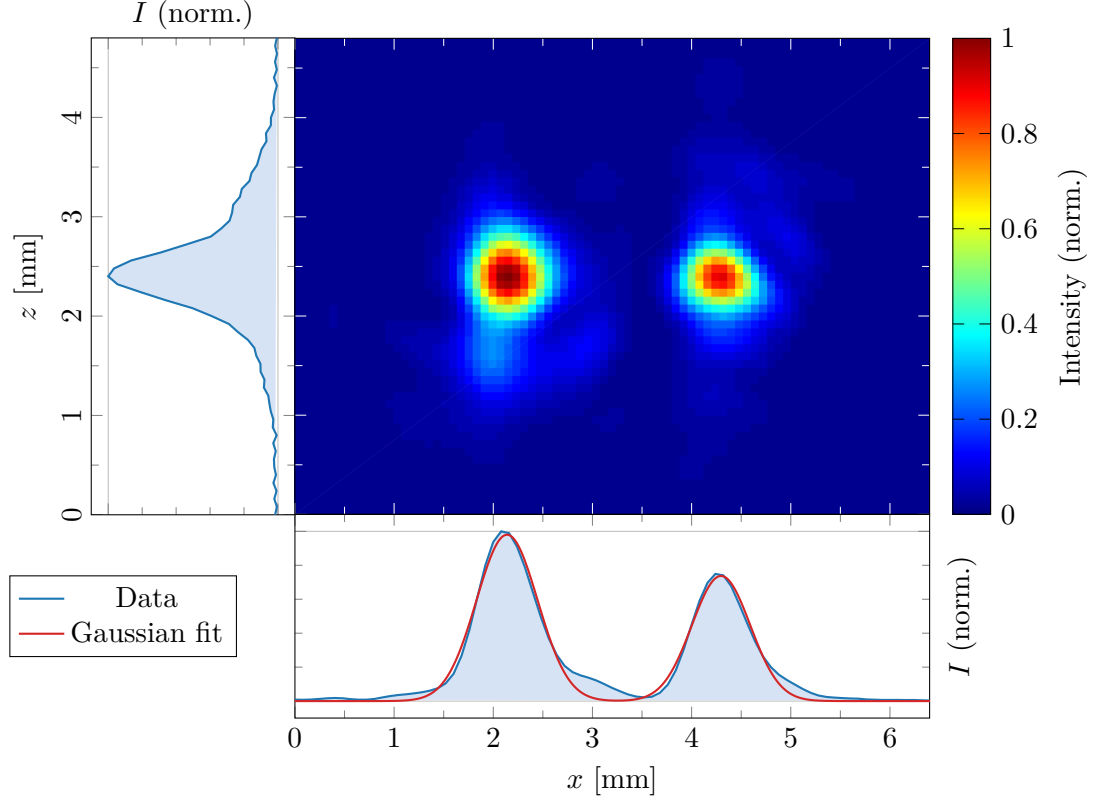


Figure 4.6. Beam profile intensity map of both excitation arms slightly out of focus with integrated intensities along the x - and z -axes. Data has been measured with a 2D array of pyroelectric solid-state detectors (Ophir Spiricon Pyrocam IV).

Beam	a	b [mm]	c [mm]
Left	0.98	2.139	0.436
Right	0.74	4.297	0.416

Table 4.3 Gaussian fit parameters of the integrated intensities along the x -direction.

5. Results

For this thesis a total of five beam times at the FHI FEL have been spent to acquire experimental data comprising SHG spectra, azimuthal scans and reflectivity spectra over the frequency range from 350 cm^{-1} to 1400 cm^{-1} . Table 5.1 gives an overview over the measurements.

Table 5.1. Measurements conducted for this thesis. The electron energy refers to the free electrons' kinetic energy in the FEL.

#	Date	Electron energy	Spectral range [cm^{-1}]
1	Sep 23, 2015	31.0 MeV	575 to 1400
2	Oct 08, 2015	31.0 MeV	650 to 1400
3	Nov 27, 2015	23.5 MeV	350 to 850
4	Feb 09, 2016	23.5 MeV	350 to 850
5	Mar 18, 2016	31.0 MeV	350 to 850

This chapter will present the results of the aforementioned experiments. Thereto, data measured at room temperature are shown first. Afterwards, the temperature dependence is shown by plotting the respective scans at different sample temperatures in the same graph followed by a description of the observed effects. All measured intensities have been divided by the reference signal (see section 4.2.1) to ensure that the data is independent of FEL power drifts and jitter.

5.1. Second Harmonic Phonon Spectroscopy

SHG spectra at room temperature and in SPP polarization were measured over the course of two beam times (#1 and #3). In order to achieve a single spectrum over the entire frequency range from 350 cm^{-1} to 1400 cm^{-1} , three separate measurements had to be merged as varying FEL energy settings and spectral filter configurations were necessary. Although spectral overlap intervals at signal-rich positions were used to match integrated signals of adjacent spectral regions, relative magnitudes of resonances might thus not be described entirely correct in this representation of the measured data. The merged spectrum is shown in figure 5.1.

Distinct peaks at TO phonon frequencies of the vibrational *E*-type modes (ordinary ray) are apparent ranging over multiple orders of magnitude ($\sim 10^{-3}$ to 10^0), primarily dominated by the resonance at Ω_6^{TO} , which is why a semi-logarithmic scale has been chosen for better visibility of all observable features. The spectrum also exhibits features in the longer-wavelength region which

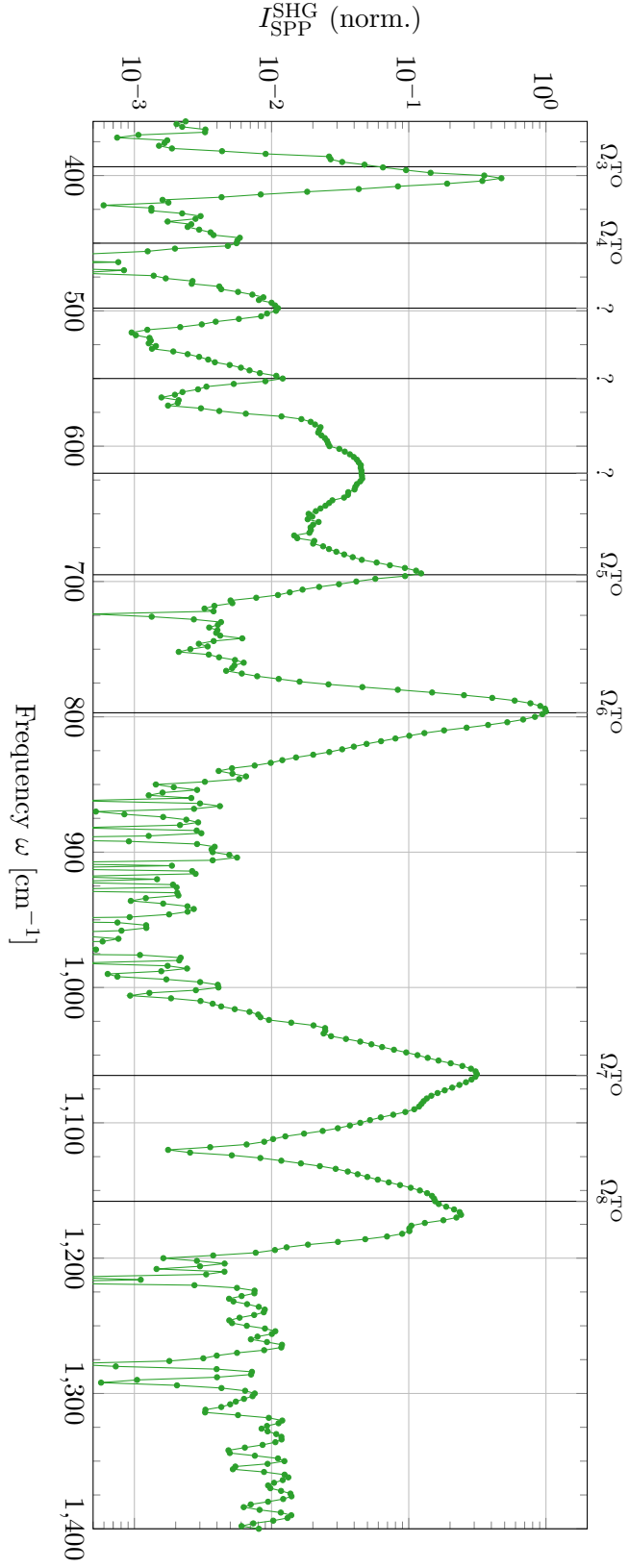


Figure 5.1. SHG spectrum for SPP polarization at room temperature. Distinct peaks mark TO phonon frequencies while three unattributed features are located in the lower-frequency region of the spectrum. Note the semi-logarithmic scale.

cannot be directly attributed to phonon resonances, i.e. sharp peaks around 498 cm^{-1} and 550 cm^{-1} as well as a broad continuum ranging from 570 cm^{-1} to 660 cm^{-1} . Possible interpretations of those features will be given in section 6.1.

5.1.1. Temperature Dependence of the SHG Spectrum

In order to see the effects of higher sample temperatures on the features caused by phonon resonances and possible indications of the $\alpha \rightarrow \beta$ phase transition of quartz at nominally $T_C = 573^\circ\text{C}$, the previously described measurements have been repeated with the sample mounted inside a probe heater as described in section 4.2.2. The experiment was conducted for five different temperatures, i.e. 28°C , 200°C , 400°C , 575°C and 650°C . The measured data is shown in figure 5.2 (note the semi-logarithmic scale).

While a general decrease in SHG intensity can be observed with increasing temperature, at phonon resonances a broadening of the peaks as well as shifts of the spectral positions are apparent. Resonances at Ω_4^{TO} , Ω_5^{TO} and Ω_6^{TO} red-shift while no clear frequency shift can be observed at Ω_3^{TO} , Ω_7^{TO} and Ω_8^{TO} . Tendencies of both broadening and the observed shifts of the peak positions concur with experimental data acquired via linear reflectivity measurements according to Gervais et al. [24].

Additionally, the transition from 575°C to 650°C seemingly causes a step-like drop of the SHG signal in some parts of the spectrum. This becomes particularly apparent when examining the resonance at Ω_8^{TO} where the resonance peak becomes gradually smaller until it disappears entirely as 573°C are exceeded. Similar behaviors can be observed at Ω_5^{TO} which suggests that the phase transition in fact occurred as those particular phonon modes are expected to become forbidden in the β -phase of quartz while at Ω_3^{TO} some intensity remains which might be due to an outgoing resonance of the non-forbidden mode at $\Omega_6^{\text{TO}} \approx 2\Omega_3^{\text{TO}}$, even though Ω_6^{TO} shifts to lower frequencies with increasing temperature, a trend that cannot be observed for the resonance at Ω_3^{TO} .

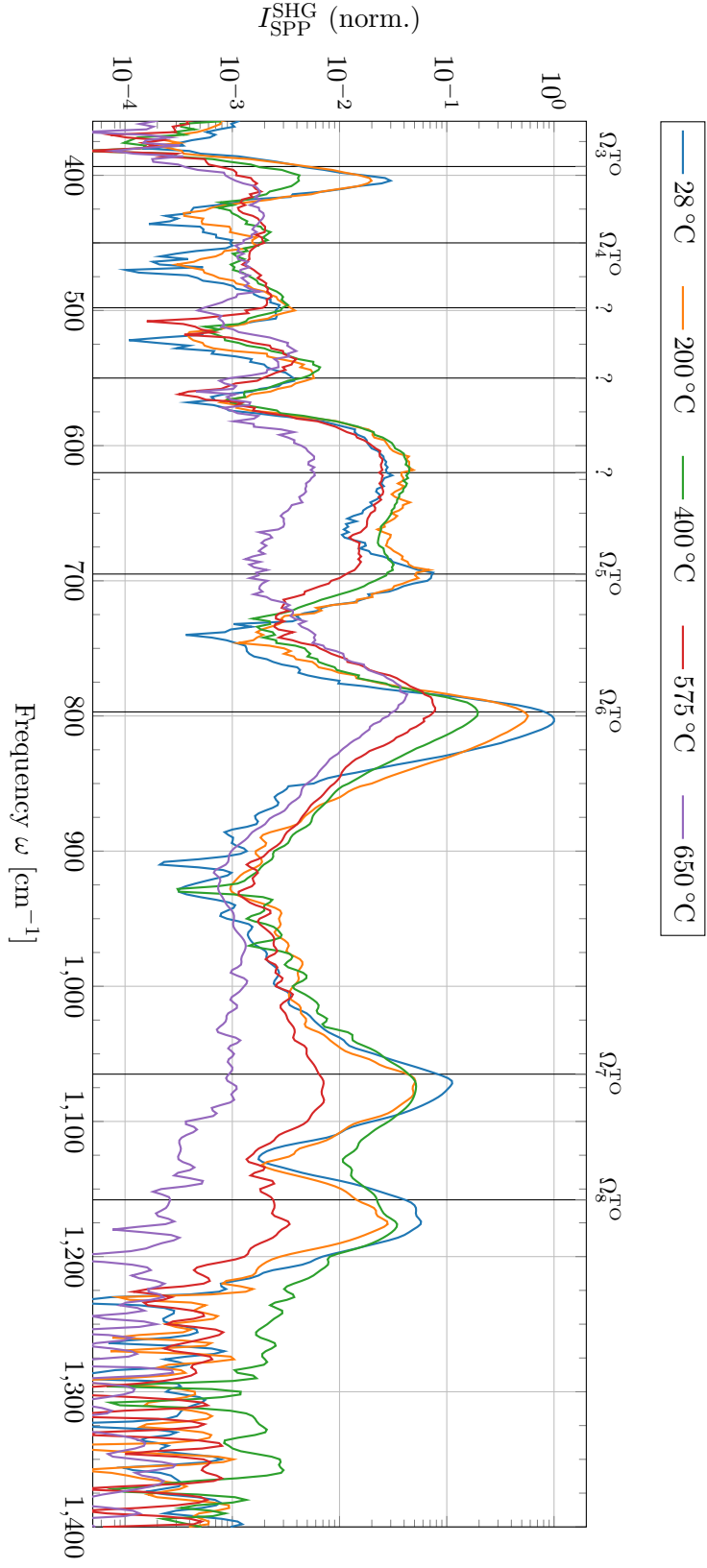


Figure 5.2. Temperature dependence of the SHG signal measured for five different temperatures ranging from room temperature up to 650 °C. With increasing temperature, phonon resonances blur out and are subject to spectral shifts. Data normalized. Note the semi-logarithmic scale.

5.2. Probing the Crystal Structure: Azimuthal SHG

In these measurements, the SHG signal for two polarization configurations, i.e. SPP and PPP, at the fixed spectral positions of four different resonances, i.e. at Ω_3^{TO} , Ω_6^{TO} , Ω_7^{TO} and Ω_8^{TO} , in the SHG spectra was detected. The results are shown in figure 5.3 and exhibit clear azimuthal dependencies in the detected SHG intensities which fit the theoretical expectations as discussed in section 3.3 nicely. For fitting, effective $\chi^{(2)}$ parameters A and B were defined to include expressions for the electric fields and Fresnel transmission coefficients according to equation 3.3.7:

$$\begin{aligned} A &= (L_{xx}E_{1,x}^i)(L_{xx}E_{2,x}^i)\chi_{aaa}^{(2)} \\ B &= [(L_{zz}E_{1,z}^i)(L_{xx}E_{2,x}^i) + (L_{xx}E_{1,x}^i)(L_{zz}E_{2,z}^i)]\chi_{acb}^{(2)}. \end{aligned} \quad (5.2.1)$$

Data were then fitted using the following fit functions:

$$\begin{aligned} I_{\text{SPP}}^{\text{SHG}}(\phi) &= |A \sin(3\phi) + Be^{i\Phi}|^2 \\ I_{\text{PPP}}^{\text{SHG}}(\phi) &= |A \cos(3\phi)|^2 \end{aligned} \quad (5.2.2)$$

where Φ introduces a relative phase between the additive terms.

As expected from theoretical considerations and simulations described in section 3.3, the shapes of the azimuthal scans vary depending on the set of parameters A and B . For example, $A \ll B$ will result in a more circular shape while $A \gg B$ would generate six rather equally sized lobes.

Simulations are in good agreement with the experimental data, except for PPP-polarization at $\Omega_6^{\text{TO}} = 800 \text{ cm}^{-1}$ where a distinct threefold symmetry of the rotational spectrum is observed while the simulation predicts a sixfold symmetry. While the data can be fitted using the model for SPP polarization, the PPP model does not yield a satisfactory fit. This mismatch will be discussed more thoroughly in section 6.3.

Table 5.2 gives the fit parameters A and B along with their ratio A/B extracted from the fits according to equation 5.2.2. No relative phase between both terms was required in order to fit the data properly. As only $\chi_{aaa}^{(2)}$ enters $I_{\text{PPP}}^{\text{SHG}}$, azimuthal scans in PPP polarization yield no information about relative magnitudes of $\chi^{(2)}$ tensor elements. It is noteworthy that apart from the symmetry also the angular positions of smaller and larger lobes are sensitive to relative $\chi^{(2)}$ magnitudes as can be exemplarily seen for the SPP scans at Ω_3^{TO} and Ω_7^{TO} where lobe amplitudes are similar but at different angular positions which results in a differently signed A/B ratio.

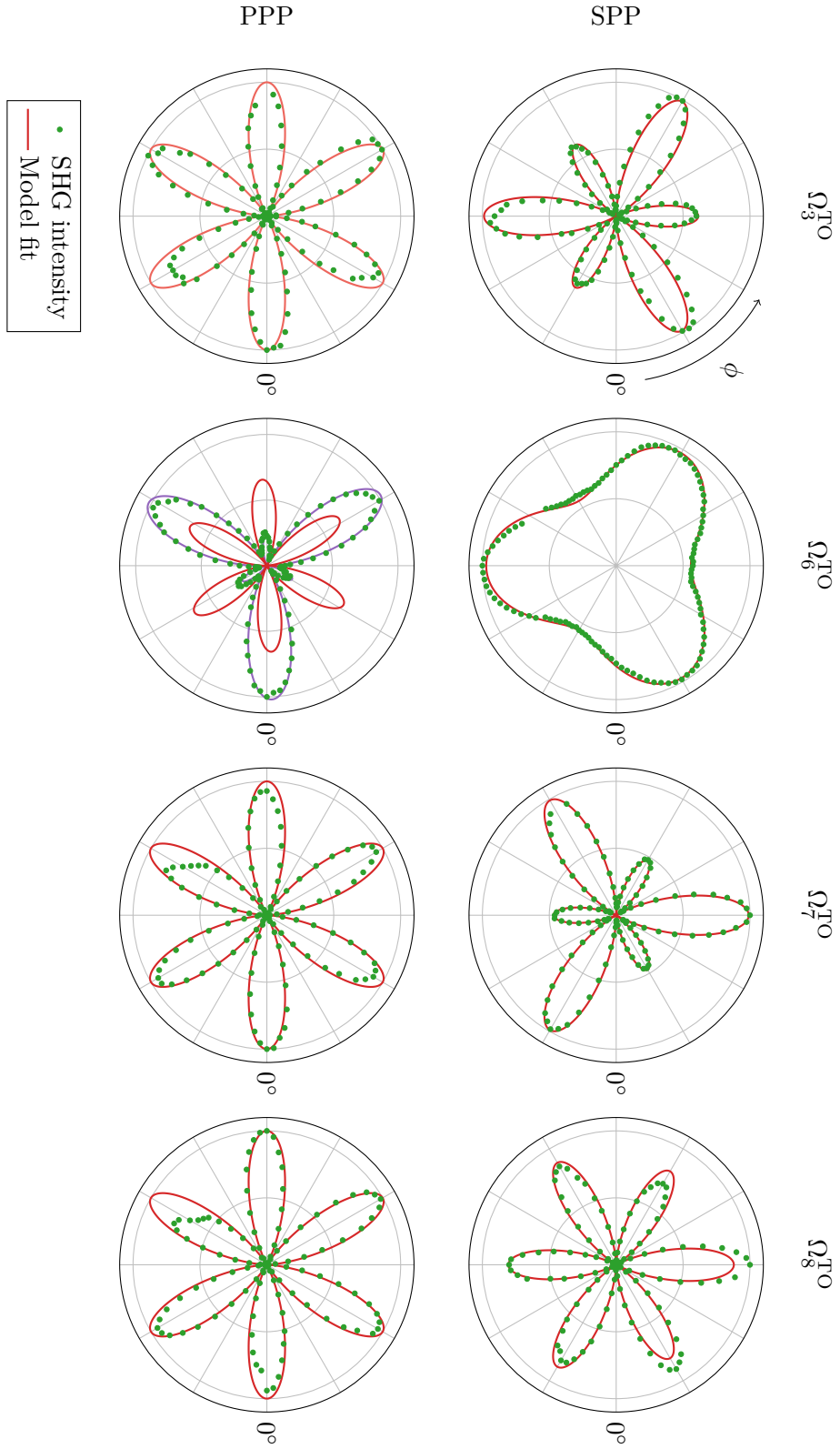


Figure 5.3. Azimuthal SHG scans for four wavelengths in both, SPP and PPP polarization configurations with fits according to functions 5.2.2. The scan at Ω_6^{TO} in PPP polarization has additionally been fitted with the SPP model (purple line). Data normalized.

Table 5.2. Fit parameters of the measured azimuthal SHG scans in SPP polarization determined using equation 3.3.7. Errors have been extracted from the applied trust region fit algorithm (95% confidence bounds).

<i>E</i> -mode	<i>A</i>	<i>B</i>	<i>A/B</i>
Ω_3^{TO}	0.89 ± 0.05	0.105 ± 0.004	8.5 ± 0.6
Ω_6^{TO}	0.120 ± 0.003	0.8657 ± 0.0020	0.14 ± 0.04
Ω_7^{TO}	0.839 ± 0.007	-0.154 ± 0.006	-5.45 ± 0.23
Ω_8^{TO}	0.919 ± 0.009	-0.021 ± 0.008	-44 ± 17

5.2.1. Temperature Dependence of the Azimuthal Scans

Also the azimuthal dependencies were measured for temperatures above room temperature up to 650 °C. Due to technical restrictions azimuthal scans could only be performed over an angular range of 80° to 100°. Normalized data with model fits are shown in figure 5.4 and fit parameters of the unnormalized data are listed in table 5.3.

At Ω_3^{TO} , a strong decrease of *A* with increasing temperature can be observed up to 575 °C. Absolute values of (negative) *B* parameters mainly decrease with temperature as well although seemingly coming to a halt at 400 °C and even slightly increase at 575 °C. The transition from 400 °C to 575 °C comes with a abrupt change in the relative phase Φ and also in the *A/B* ratio which increases nearly by a factor of 4. At 650 °C no SHG signal could be detected.

The vibrational phonon mode at Ω_6^{TO} yielded SHG signal up to 650 °C and exhibits a much more gradual behavior of all fit parameters with no clear indication of a phase transition.

At Ω_7^{TO} , *A* gradually decreases, while *B* approaches zero, resulting in a decrease of the *A/B* ratio up to 400 °C until it suddenly increases and with the SHG signal the azimuthal dependence ultimately breaks off at 650 °C.

Azimuthal scans at Ω_8^{TO} show similar amplitudes of small and large lobes which corresponds to a regime where $A \gg B$ which is less sensitive to relative changes of the $\chi^{(2)}$ contributions. Therefore relative errors are high and no clear trend with increasing temperature can be determined other than a general decrease of SHG intensity with rising temperature. At 575 °C the SHG signal down.

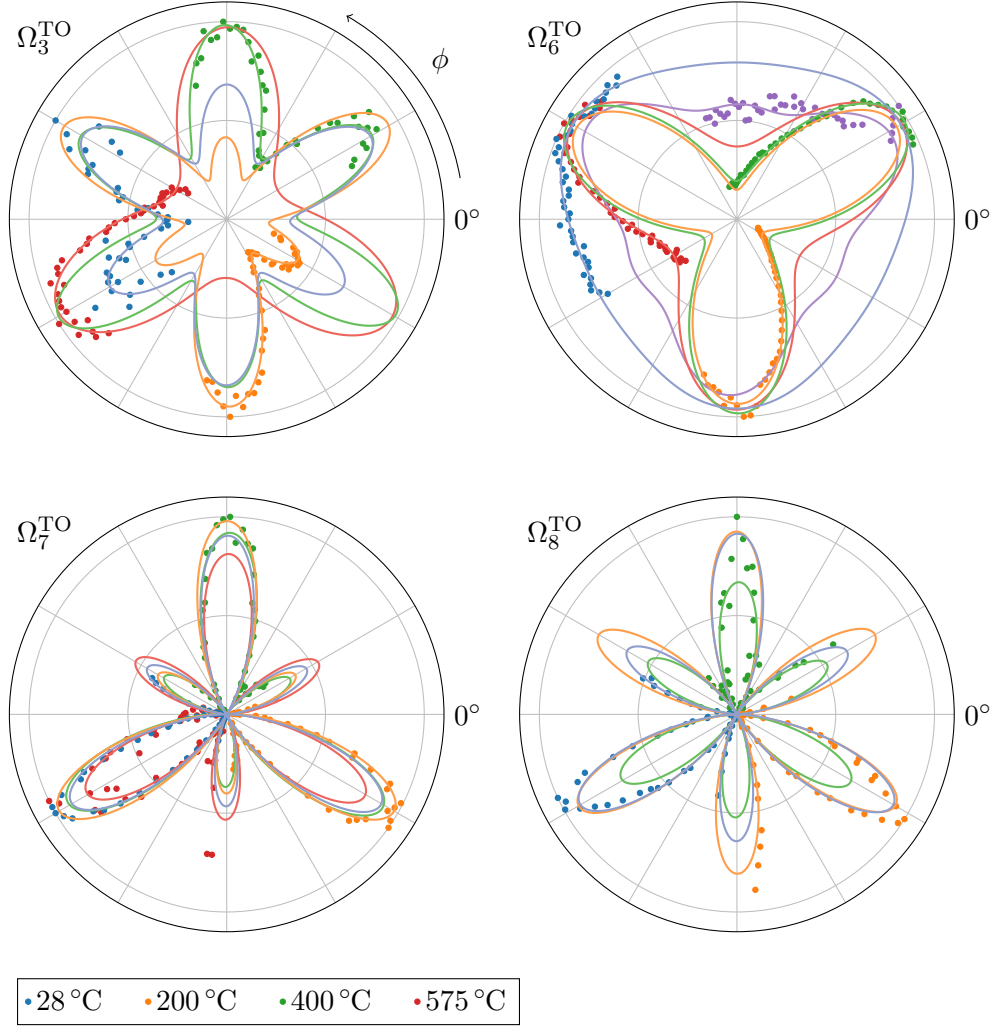


Figure 5.4. Temperature dependent azimuthal SHG scans for four wavelengths in SPP polarization. Data has been normalized and rotated by multiple integers of 120° (as per symmetry) for better visibility. Dots mark the experimental data (normalized) while solid lines mark the model fits.

Table 5.3. Fit parameters of the measured azimuthal SHG scans in SPP polarization determined using 3.3.7. Errors have been extracted from the trust region algorithm (95% confidence bounds).

E -mode	T [°C]	A	B	Φ	A/B
Ω_3^{TO}	28	0.66 ± 0.06	-0.57 ± 0.05	1.47 ± 0.15	-1.15 ± 0.15
	200	0.280 ± 0.012	-0.217 ± 0.012	1.16 ± 0.03	-1.29 ± 0.10
	400	0.113 ± 0.005	-0.091 ± 0.004	1.65 ± 0.03	-1.24 ± 0.08
	575	0.058 ± 0.009	-0.119 ± 0.004	2.32 ± 0.12	-4.87 ± 0.05
	650	No SHG signal			
Ω_6^{TO}	28	0.15 ± 0.09	0.924 ± 0.011	1.88 ± 0.20	0.16 ± 0.10
	200	0.20 ± 0.04	0.377 ± 0.014	2.67 ± 0.26	0.53 ± 0.11
	400	0.106 ± 0.020	0.215 ± 0.009	2.58 ± 0.26	0.49 ± 0.10
	575	0.051 ± 0.012	0.136 ± 0.004	2.32 ± 0.20	0.38 ± 0.09
	650	0.043 ± 0.014	0.104 ± 0.006	1.87 ± 0.13	0.41 ± 0.14
Ω_7^{TO}	28	0.817 ± 0.026	0.13 ± 0.08	0 ± 3000	6 ± 4
	200	0.516 ± 0.014	0.151 ± 0.024	0.68 ± 0.18	4.7 ± 0.6
	400	0.404 ± 0.019	0.132 ± 0.024	0.76 ± 0.18	4.6 ± 0.6
	575	0.212 ± 0.019	0.06 ± 0.04	1.17 ± 0.26	7.4 ± 2.4
	650	No SHG signal			
Ω_8^{TO}	28	0.877 ± 0.026	0.10 ± 0.12	0.6 ± 1.6	9 ± 11
	200	0.82 ± 0.03	0.04 ± 0.48	0 ± 2100	24 ± 250
	400	0.45 ± 0.05	0.03 ± 0.31	1 ± 14	10 ± 155
	575	No SHG signal			
	650	No SHG signal			

5.3. Linear Spectroscopy: Reflectivity

Simultaneously and complementary to the nonlinear SHG spectra, linear measurements of the reflectivity in dependence of the FEL frequency have been conducted at a reflection angle of 60° using a pyroelectric detector. Results for the P- and S-polarized beams are shown in figure 5.5.

Both spectra are dominated by two pronounced Reststrahlen regions, i.e. regions of particularly high reflectance, ranging from approximately 450 cm^{-1} to 510 cm^{-1} and from 1065 cm^{-1} to 1300 cm^{-1} which are due to large TO-LO phonon splittings of the respective vibrational modes (Ω_4^{TO} and Ω_7^{TO}). Apart from these prominent features, smaller but distinct features around TO resonance frequencies Ω_3^{TO} , Ω_5^{TO} and Ω_6^{TO} can be observed. As these phonon modes have a much smaller TO-LO splitting (see section 2.3.2), their dedicated features appear much sharper in the spectra. The spectral feature associated with the phonon mode around Ω_8^{TO} shows a different behavior as it is located between Ω_7^{TO} and Ω_7^{LO} and thus inside the corresponding Reststrahlen region. Also, it has a smaller TO-LO splitting and thus a small oscillator strength. As a result it causes a pronounced dip in the Reststrahlen band between Ω_7^{TO} and Ω_7^{LO} .

Generally, the applied model as discussed in section 3.2 describes the experiment satisfactorily well as fit functions are in fair accordance with experimental data. The measured data have been fitted with fixed phonon frequencies and dampings according to [24] with the sample temperature as a free fit parameter. Fitted temperatures were

$$\begin{aligned} T_P &= (67 \pm 24)^\circ\text{C} \\ T_S &= (35 \pm 23)^\circ\text{C} \end{aligned} \tag{5.3.1}$$

with errors calculated from the trust region fit algorithm (95% confidence bounds). Nonetheless, a few characteristics of the measured spectra do not seem to be modeled accurately by the simulation, especially in the pronounced Reststrahlen regions where reflectance is high. Compared to the model, measured reflectivity drops towards the red and blue ends of the lower and higher Reststrahlen bands, respectively. This mismatch might be caused by nonperfect filter transmission which becomes more noticeable at high reflectivities although unknown physical reasons cannot be ruled out as well.

5.3.1. Temperature Dependence of the Reflectivity Spectrum

Reflected intensities in P-polarization were also measured in dependence of the sample temperature. The measured data are shown in figure 5.6. Effects of the increasing sample temperature on the reflectivity are clearly visible in the spectra. While the reflected intensities taper off in general, some features in the spectrum disappear almost entirely like peaks at Ω_3^{TO} and Ω_5^{TO} as well the dip at Ω_8^{TO} in the upper Reststrahlen region. This is in accordance with the fact that the E -modes with $j = 3, 5, 8$ are expected to become forbidden as quartz enters its β -phase at $T_C = 573^\circ\text{C}$. All observable features experience a spectral broadening due to increasing damping coefficients as expected [24].

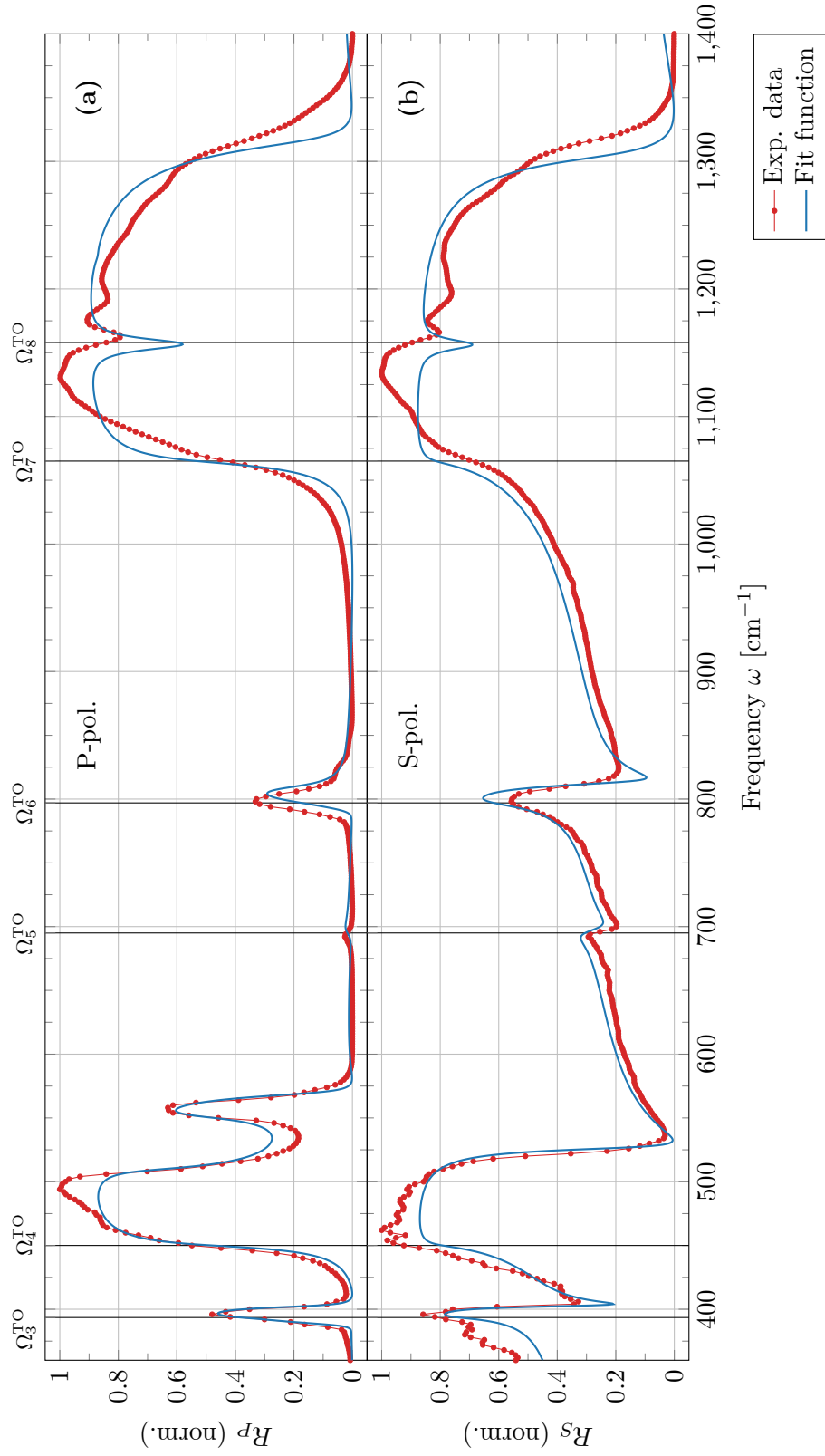


Figure 5.5. Reflectivity spectra at room temperature for (a): P-polarized and (b): S-polarized beams together with respective fit functions as described in section 3.2.

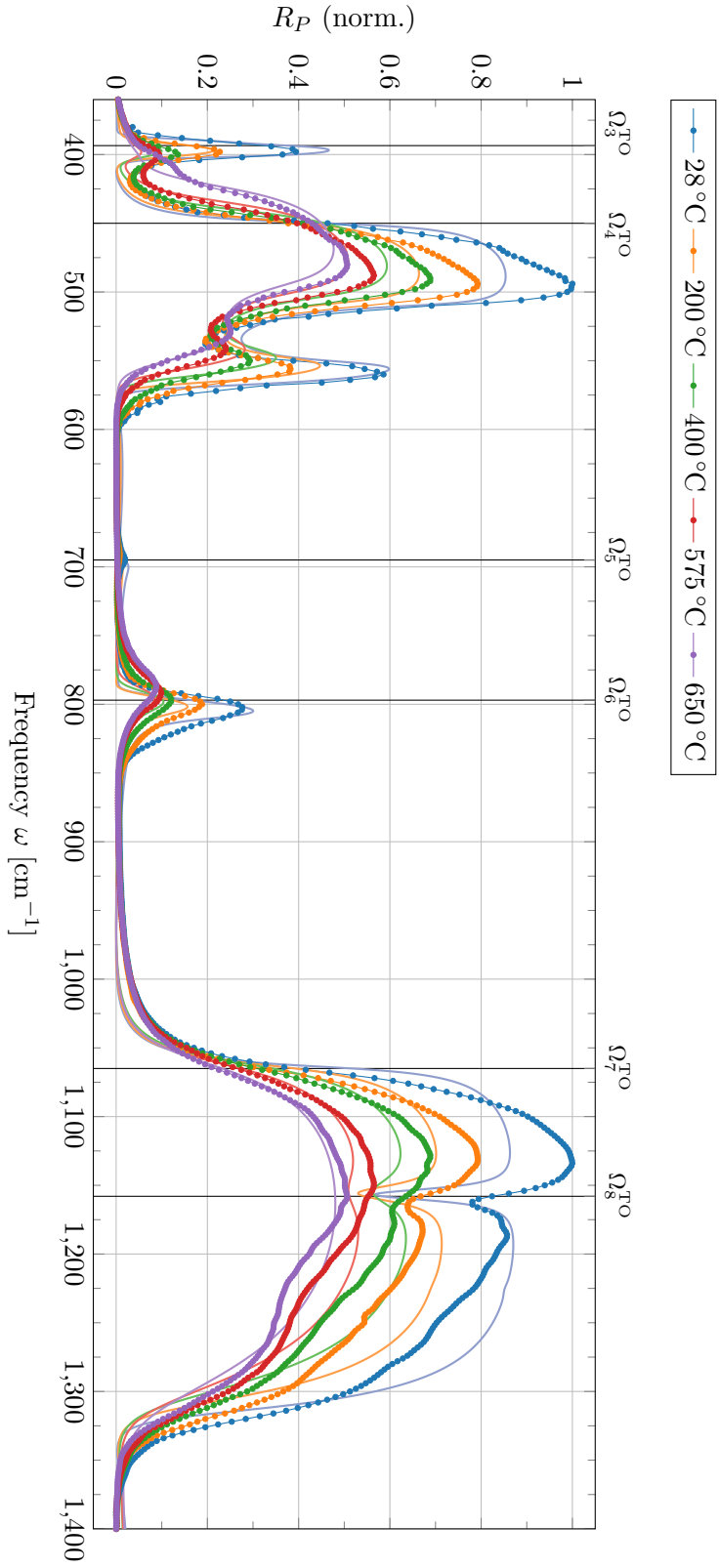


Figure 5.6. Temperature dependence of the reflectivity in P-polarization measured for five different temperatures ranging from room temperature up to 650 °C.

The measured reflectivity spectra have been fitted with temperature-dependent phonon data taken from reference [24] leaving the sample temperature as the only free fitting parameter. Results of these fits are listed in table 5.4.

T_{set} [°C]	T_{fit} [°C]
28	49 ± 24
200	212 ± 25
400	377 ± 20
575	496 ± 15
650	653 ± 10

Table 5.4 Fit parameters of the reflectivity model as described in section 3.2 to the measured temperature-dependent spectra. Errors have been extracted from the trust region algorithm (95% confidence bounds).

All fitted temperatures coincide with their respective nominal set temperatures within or close to single error suggesting that the temperature measured by the feeler gauges inside the probe heater matches the actual sample temperature satisfactorily.

While the applied model generally describes the experimental results quite well, it struggles to fit the behavior of the high reflectivity in the Reststrahlen bands as already observed for the measurement at room temperature.

6. Discussion

This chapter refers to the experimental results presented in the preceding chapter and aims to assess and interpret the acquired data as well as to give physical explanations of the observed effects.

Thereto, interpretations of the measured SHG spectra are given along with possible improvements of the applied analysis methods. Afterwards, a comparison of SHG spectroscopy with linear reflectivity measurements is given comprising an analysis of temperature dependencies for both techniques. This is followed by a treatment of the unexpected behavior of the phonon mode at Ω_6^{TO} . Ultimately, a possible phase transition from α -quartz to β -quartz is discussed based on the acquired results.

6.1. Interpretation of SHG Spectra

The SHG spectrum at room temperature shows distinct peaks at frequencies coinciding with the TO phonon resonances for the E -modes (ordinary ray) of quartz. While all resonances associated with the E -modes could be identified in the spectrum, there is no indication of A_2 -type modes in the data, suggesting that these measurements are solely sensitive to vibrational modes perpendicular to the optic axis. This is most likely due to the fact that Fresnel transmission coefficients tend to take very small values at phonon resonances parallel to the optic axis [3], therefore strongly suppressing SHG signal at those resonance frequencies.

The reason for the enhancement of the SHG signal at TO phonon resonances becomes more clear when considering equation 2.2.10. Denominators $D(\omega)$ become very small as the excitation wavelength approaches the TO phonon resonance causing an enhancement of the respective term and ultimately of the second-order electric susceptibility $\chi^{(2)}$ which itself affects the measured SHG intensity as described by equation 2.0.1.

Apart from peaks directly attributed to TO phonon resonances, three clear features of unknown origin could be observed: Two sharp peaks at 498 cm^{-1} and 550 cm^{-1} as well as one broad continuum ranging from approximately 570 cm^{-1} to 660 cm^{-1} . A possible explanation for SHG enhancement aside from direct phonon resonances in the lower-frequency region could be provided by outgoing resonances of higher frequency modes which arise from the $1/D(\omega_1 + \omega_2)$ term in equation 2.2.10. For SHG, we have $\omega_1 = \omega_2$ and thus outgoing resonances are expected at half the incoming resonances' frequencies. $\Omega_7^{\text{TO}}/2 = 533\text{ cm}^{-1}$ and $\Omega_8^{\text{TO}}/2 = 579\text{ cm}^{-1}$ match those unattributed sharp features by a discrepancy of 35 cm^{-1} and 29 cm^{-1} , respectively. Another possibly more likely source for

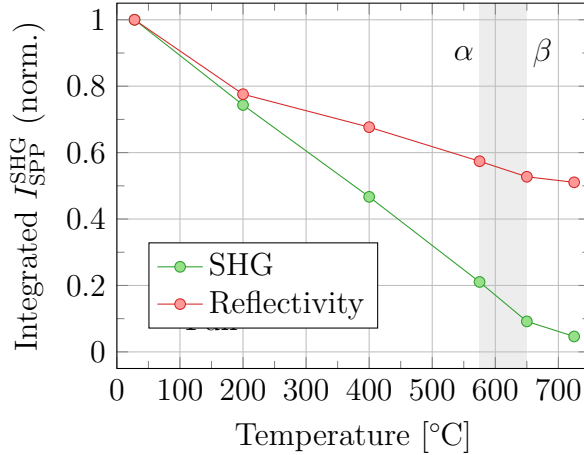
the SHG enhancement at those frequencies are the highly dispersing Fresnel transmission coefficients which can also be responsible for distinct features in the spectra. Furthermore, the exact origin of the broad continuum around 620 cm^{-1} remains unclear. While an association with the phonon mode at Ω_5^{TO} is possible, it is noteworthy that unlike the adjacent phonon mode, the broad feature does not wear off at temperatures higher than T_C .

For a complete and thorough interpretation of the SHG spectra, it is necessary to establish the theoretical framework to model the dispersion of the second-order electric susceptibility $\chi^{(2)}(\omega)$. Due to the multitude of free parameters which is owed to the generalization of Flytzanis' model [19] to multiple phonon resonances as sketched in section 2.2.2, reasonable approximations might be necessary to apply the modified equations for fitting. One possible approach would be to use the generalized $\chi^{(2)}(\omega)$ dispersion and neglect a majority of the occurring cross-terms to reduce the model to the mainly contributing terms. Additionally, a full treatment of Fresnel transmission coefficients is necessary as those are highly dispersive in the vicinity of phonon resonances.

6.2. Nonlinear vs. Linear Measurements

One reason to measure the reflectivity along with the SHG spectra was to compare the novel nonlinear approach of second harmonic phonon spectroscopy to already established linear techniques as reflectance spectroscopy, especially with regard to temperature sensitivity and response to the phase transition. For better comparison, both SHG and reflectivity signals have been integrated over selected frequency intervals to determine each of those techniques' temperature-dependent behaviors. Temperature kinetics over the whole spectral range are shown in figure 6.1.

Figure 6.1 Temperature dependence of SHG and reflectivity intensities integrated over the entire spectral range. Data normalized.



From the data it becomes clear that SHG measurements exhibit a significantly higher contrast in the temperature dependence as linear reflectance measurements do. Thus, SHG spectroscopy can be considered more sensitive to changes in the sample temperature. While SHG intensities decrease in a very linear man-

ner throughout the entire temperature range up to T_C , reflectivity exhibits a clear kink at the 200 °C point and continues linearly from there. At T_C however, the SHG curve displays a significant change in its slope while the reflectivity's trend remains largely the same implying that nonlinear SHG measurements are also more sensitive to the phase transition at T_C in terms of intensity.

To distinguish different signal contributions from individual spectral features, integrated intensities over different frequency intervals have been extracted that can be associated with particular peaks in the spectra like phonon resonances and also unattributed features like the broad continuum around 620 cm^{-1} . Individual integration intervals are listed in table 6.1 and the respective plots are shown in figure 6.2.

Feature	Integration interval [cm^{-1}]
Ω_3^{TO}	384 to 426
Ω_5^{TO}	688 to 698
Ω_6^{TO}	746 to 856
Ω_7^{TO}	1052 to 1096
	1070 to 1074
Ω_8^{TO}	1152 to 1194
	1168 to 1174
Continuum	578 to 658

Table 6.1 Integration intervals for the temperature kinetics of SHG and reflectivity spectra. For Ω_7^{TO} and Ω_7^{TO} additional narrow intervals have been chosen to compare peak broadness versus peak amplitude.

For all integration intervals, except for the continuum where the reflectivity is essentially featureless, SHG curves show a much larger contrast than reflectivity curves affirming the previous conclusion that SHG spectroscopy is more temperature-sensitive than reflectance spectroscopy, also at individual features.

At phonon modes that are expected to become forbidden in quartz's β -phase, i.e. Ω_3^{TO} , Ω_5^{TO} , Ω_7^{TO} and Ω_8^{TO} , SHG curves exhibit a nearly flat curve shape beyond T_C while simultaneously dropping to nearly zero intensity and therefore leaving a kink around T_C . An exception to this constitutes the phonon mode at Ω_3^{TO} which, although being flat, retains a significant amount of remaining intensity. A possible reason for that effect, might be the fact that the mode at Ω_6^{TO} , a non-disappearing mode, has an outgoing resonance around Ω_3^{TO} as $\Omega_6^{\text{TO}} \approx 2\Omega_3^{\text{TO}}$. In contrast, at Ω_6^{TO} no observable change except for a continuation of the gradual decrease in intensity is apparent at T_C which concurs with the fact that this mode is supposed to survive the phase transition.

A peculiar behavior of the SHG intensity can be observed at Ω_7^{TO} and Ω_8^{TO} where the SHG intensity at 400 °C is higher than at 200 °C. Additionally, smaller integration windows at the respective peak positions have been chosen. The value at 400 °C is clearly smaller for the narrow integration interval (dashed line) implying that these peaks primarily gain in width rather than in amplitude as the sample temperature rises.

The continuous feature scales in a very nonlinear fashion with temperature before T_C and exhibits a relatively flat curve shape beyond T_C similar to other features that wear off after the phase transition. It can thus be concluded that

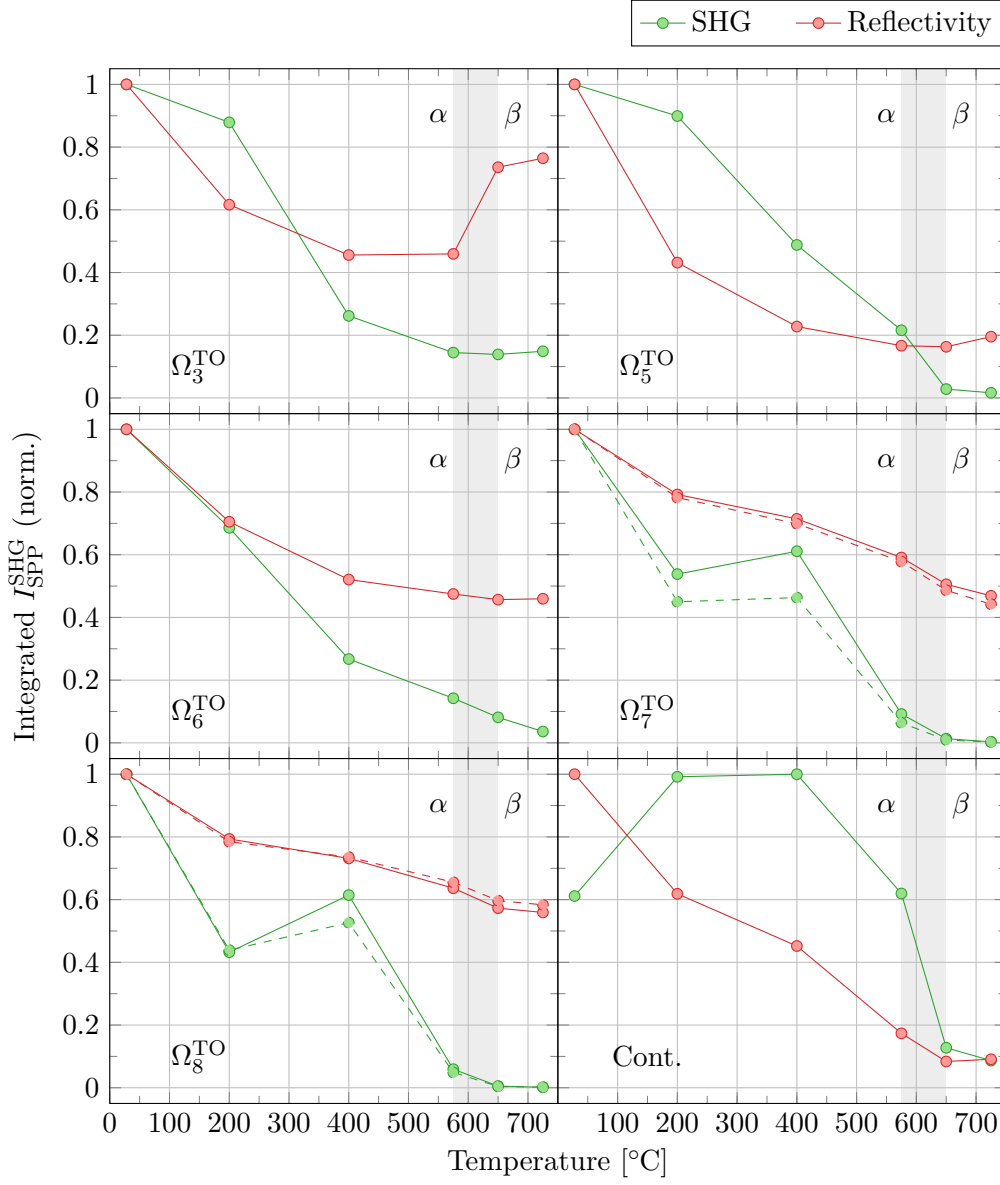


Figure 6.2. Temperature dependence of SHG and reflectivity. Signals have been integrated over frequency intervals that include particular features of the spectra. For Ω_7^{TO} and Ω_8^{TO} additional narrow intervals has been plotted (dashed lines). The plots suggest that the phase transition occurs between 575 °C and 650 °C (gray shade). Data normalized.

the unattributed continuous feature gets affected by the $\alpha \rightarrow \beta$ phase transition and might possibly even be associated with the adjacent resonance at Ω_5^{TO} .

Unlike the SHG intensities, reflectivity displays very little to no change in curve shape at the phase transition. A seemingly phase change-induced effect occurs at Ω_3^{TO} where reflectivity starts to rise beyond T_C . In fact, this increase in reflectivity intensity is due to a broadening of the adjacent Reststrahlen region associated with Ω_4^{TO} and the subsequent intensity “leakage” into the neighboring feature and thus constitutes no real phase transition-induced effect. On the one hand, this allows for the conclusion that intensity-wise SHG spectroscopy is a more phase transition-sensitive tool. On the other hand, it has been shown that reflectivity measurements turned out to be very sensitive to the $\alpha \rightarrow \beta$ phase transition of quartz when tracking spectral positions and dampings of phonon resonances as the temperature increases [24], an approach that has not been employed for SHG spectroscopy in the scope of this thesis but might yield additional insight.

6.3. Anomaly at Ω_6^{TO}

The phonon resonance at Ω_6^{TO} shows an unexpected behavior in two ways. First, the azimuthal scan in PPP polarization exhibits a clear threefold symmetry, while this configuration is expected to yield a sixfold symmetric azimuthal shape. Secondly, temperature-dependent measurements under SPP polarization conditions revealed that this phonon mode retains a clear azimuthal dependence, even well above the phase transition temperature. This behavior does not match the theoretical expectations for β -quartz and adds to the peculiarity of this phonon mode.

The origin of this mismatch is yet to be investigated. A possible explanation could be the presence of a surface mode on the sample which, due to the broken symmetry along the surface normal, exhibit different symmetry relations in the $\chi^{(2)}$ elements and therefore a different azimuthal behavior (see section 3.3.1). The observed threefold symmetric dependence of the SHG signal on the azimuthal angle in PPP polarization is in accordance with the expected C_{6v} symmetry (sixfold about optic axis) at the surface [6] which has been confirmed by low-energy electron diffraction (LEED) [37] and helium atom scattering (HAS) [38] studies. Given that the threefold symmetric modulation of the SHG signal is in fact due to surface vibrational modes, it still remains unclear why the expectedly weak SHG signal coming from surface modes (compared to bulk modes) would have such a strong effect on the measured signal as surface contributions involve only a surface-near layer and therefore a much smaller number of oscillators.

6.4. $\alpha \rightarrow \beta$ Phase Transition of Quartz

Results presented in this thesis reveal multiple indications of the $\alpha \rightarrow \beta$ phase transition of quartz. Firstly, temperature-dependent SHG spectra as presented in section 5.1.1 show step-like changes in their SHG intensities at those spectral features which belong to β -forbidden phonon modes of quartz. These abrupt intensity drops occur between the measurement points at 575 °C and 650 °C, i.e. shortly after the nominal transition temperature $T_C = 573$ °C. These effects also manifest in the temperature dependence of the integrated intensities shown in section 6.2 where it becomes clear that SHG curves measured at β -forbidden features experience an intensity drop to almost zero beyond T_C . For reflected intensities no similar behavior could be observed.

Secondly, temperature-dependent azimuthal scans also suggest that the phase transition took place between nominal set temperatures between 575 °C and 650 °C. Scans at Ω_3^{TO} and Ω_8^{TO} lost all detectable SHG signals at 650 °C and 575 °C, respectively, while the SHG signal at Ω_7^{TO} showed a similar behavior, even though the latter is allowed in the β -phase. Considering the heavy temperature-induced broadening of the phonon mode at Ω_7^{TO} which might have led to the loss of detectable SHG signal, these observations still allow for the interpretation that quartz's $\alpha \rightarrow \beta$ phase transition actually took place. Furthermore, fit parameters show strong indications of a phase transition as effective $\chi^{(2)}$ terms, A , B , and/or their relative phase Φ change abruptly at T_C .

Only the phonon mode at Ω_6^{TO} , one of the two β -allowed phonon mode amongst those being studied with azimuthal scans, retained a clear azimuthal dependence over all measured temperature points although no azimuthal dependence is expected from β -quartz (see section 3.3.2). In that sense, azimuthal scans carry ambiguous interpretations. Most phonon modes lose their azimuthal dependencies at the phase transition but since these phonon modes at the same time also drop down to nearly zero intensity, the significance of azimuthal measurements is compromised. On the other hand, at Ω_6^{TO} a strong azimuthal dependence persists even after the phase transition.

7. Summary & Outlook

In this thesis a novel approach on studying phonon resonances in non-centrosymmetric materials has been successfully employed. For that, a non-collinear autocorrelator setup which facilitates simultaneous SHG spectroscopy and reflectivity measurements, has been designed and built. Additionally, the use of a probe heater in combination with a rotation mount has been established enabling temperature- and azimuthal angle-dependent measurements. The experiment benefited from the FHI FEL as a light source which provides tunable, narrow-band and intense mid-IR picosecond laser pulses. Quartz served as a model system to explore the means that this novel spectroscopy technique provides. Characteristic properties of quartz have been exploited to demonstrate possible advantages of second harmonic phonon spectroscopy, including very high sensitivity to phonon resonances, azimuthal dependence of the SHG intensity offering access to the crystal symmetry and thus to contributing $\chi^{(2)}$ tensor elements as well as sensitivity to changes of the material's crystal phase.

The measured spectra clearly indicate that second harmonic generation in mid-IR indeed constitutes a viable means of spectroscopically probing phonon resonances in non-centrosymmetric materials as well as their crystal structure. Its nonlinear nature advantageously cause particularly sharp peaks at phonon resonances as well as features that cannot directly be attributed to phonon modes which remain of unknown origin up to this point but might provide additional information in the future. Azimuthal scans were largely in accordance with theoretical expectations except for the phonon mode at Ω_6^{TO} which exhibited an unexpected behavior. Scans in PPP polarization revealed a clear threefold symmetry while a sixfold symmetry was expected. Also temperature-dependent measurements at Ω_6^{TO} in SPP polarization unexpectedly showed a persistence of the azimuthal dependency well above the phase transition temperature. These results suggest that there are still physical effects involved in this phonon mode which are yet to be investigated. Furthermore, complementary reflectivity measurements have been employed. These measurements were in satisfactory agreement with theoretical calculations in such a way as to enable data fitting to extract actual sample temperatures. Compared to SHG spectroscopy, linear reflectance measurements turned out to be less temperature-sensitive in terms of intensity and showed very little sensitivity to the sample's phase transition in the integrated intensities, while considerable indications of a phase transition could be observed with the nonlinear SHG technique.

For a more complete understanding and better interpretation of the data, a working model describing the second-order nonlinear susceptibility's dispersion $\chi^{(2)}(\omega)$ at multiple phonon resonances needs to be developed. A practicable way to do this could be to adopt Flytzanis' theoretical framework [19] and extend it

7. Summary & Outlook

to multiple phonon resonances and apply reasonable simplifications like ignoring scarcely contributing cross-terms. Additionally, to fully model the SHG spectra, a complete treatment of Fresnel transmission coefficients is required.

In order to better understand the temperature-dependent behavior of the material, fitting functions could be applied to the reflectivity data such that instead of sample temperature, phonon frequencies and dampings are fitted. This would enable studies of the temperature dependence of these quantities which might yield additional insight and indications of the phase transition. Also, peak positions and widths in the SHG spectra could be tracked to possibly see indications of the material's structural change.

While quartz has proved to be a very suitable candidate to demonstrate the capabilities of second harmonic phonon spectroscopy, a clear long-term goal of these experiments is to move away from model systems and apply these newly introduced techniques to more interesting material systems. In order to study phase transitions, it would be highly beneficial to approach materials whose phase transition takes place at much lower temperatures as quartz's high transition temperature caused a heavy broadening of phononic features which made SHG detection at temperatures near T_C and above difficult. A lower transition temperature would allow for investigations of structural changes in the material while phononic features remain sharp.

A. Gaussian Beams

A.1. Description

In order to describe the propagation of a laser beam in vacuum, it is highly advisable to consider Maxwell's equations which in vacuum, i.e. in the absence of currents ($\mathbf{J} = 0$) and charges ($\rho = 0$), take the considerably simplified form (cf. equation 2.1.1):

$$\begin{aligned}\nabla \times \mathbf{E} &= -\frac{1}{c} \frac{\partial \mathbf{B}}{\partial t}, \\ \nabla \times \mathbf{B} &= \frac{1}{c} \frac{\partial \mathbf{E}}{\partial t}, \\ \nabla \cdot \mathbf{E} &= 0, \\ \nabla \cdot \mathbf{B} &= 0.\end{aligned}\tag{A.1.1}$$

With the vector identity $\nabla \times (\nabla \times \mathbf{X}) = \nabla(\nabla \cdot \mathbf{X}) - \nabla^2 \mathbf{X}$, taking the curl of the first two equations of A.1.1 yields the wave equations for the electric and magnetic field [39]:

$$\nabla^2 \mathbf{E} = -\frac{1}{c^2} \frac{\partial^2 \mathbf{E}}{\partial t^2} \quad \text{and} \quad \nabla^2 \mathbf{B} = \frac{1}{c^2} \frac{\partial^2 \mathbf{B}}{\partial t^2}.\tag{A.1.2}$$

One possible solution for the wave equation A.1.2 is the spherical wave which takes the following form for the electric field:

$$\mathbf{E}(\mathbf{r}, t) = \mathbf{A}(\mathbf{r}, t) \frac{e^{-i(\omega t - \mathbf{k} \cdot \mathbf{r})}}{|\mathbf{k} \mathbf{r}|}.\tag{A.1.3}$$

For lasers, we can assume a high degree of spatial coherence, meaning that we can solely consider that part of the spherical wave that is near the longitudinal axis ("paraxial") and beams that are axially symmetric about the axis of propagation which we define as the z -axis [40]. With these assumptions, we can define a single transverse coordinate ρ , set $\mathbf{k} \mathbf{r} = kr$ and since $\rho \ll z, r$, apply the so-called Fresnel approximation, i.e. a Taylor series about $\rho = 0$ up to first order [39]:

$$r = \sqrt{z^2 + \rho^2} \simeq z + \frac{\rho^2}{2z}.\tag{A.1.4}$$

With these approximations, the spatial representation of the wave equation A.1.2 reads:

$$\mathbf{E}(\mathbf{r}) = \frac{\mathbf{A}(\mathbf{r})}{|\mathbf{k} \mathbf{r}|} e^{i \mathbf{k} \cdot \mathbf{r}} \simeq \frac{\mathbf{A}(z, \rho)}{kz} \exp\left(i \frac{k \rho^2}{2z}\right) e^{ikz}\tag{A.1.5}$$

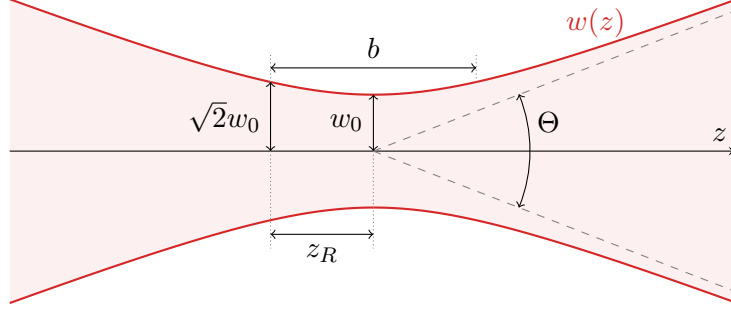


Figure A.1. A Gaussian beam's width profile $w(z)$ near the beam waist. The beam shape can be completely characterized either by its waist size $w_0 = w(0)$ and its Rayleigh range $z_R = b/2$, or by the real and imaginary parts of $q(z)$.

which has a substantial similarity to a plane wave except for a phase shift $\exp(ik\rho^2/2q)$ called the Fresnel factor. Assuming a constant amplitude $\mathbf{A}(z, \rho) = \mathbf{A}_0$ and carrying out the complex substitution $z \rightarrow q(z) = z - iz_R$ (with z_R being a real number) yields [39]:

$$\mathbf{E}(z, \rho) \simeq \frac{\mathbf{A}_0}{kq(z)} \exp\left(i \frac{k\rho^2}{2q(z)}\right) e^{ikz} \quad (\text{A.1.6})$$

which is known as the fundamental transverse electromagnetic mode or TEM_{00} mode. With

$$\frac{1}{q(z)} = \frac{z + iz_R}{z^2 + z_R^2} = \frac{1}{R(z)} + i \frac{2}{kw(z)^2}, \quad (\text{A.1.7})$$

the Fresnel factor of A.1.6 can be split into its real and imaginary parts in the following way [39]:

$$\exp\left(i \frac{k\rho^2}{2q(z)}\right) \rightarrow \exp\left(i \frac{k\rho^2}{2R(z)}\right) \exp\left[-\left(\frac{\rho}{w(z)}\right)^2\right] \quad (\text{A.1.8})$$

where the complex part is a phase factor describing the wave fronts' curvature while the real part characterizes the beam profile. From this form, we can read out a few characteristic parameters that describe the beam's properties which are also shown in figure A.1 where the beam intensity $I(z, \rho) \propto |\mathbf{E}(z, \rho)|^2$ is plotted.

A.2. Beam Parameters

For practical work with lasers, there are a few important parameters describing the Gaussian beam. Those are:

Beam width The beam width $w(z)$ corresponds to the spot size (defined as the radius at which the field amplitude falls to $1/e$ of their axial value) at

position z along the beam axis. For a beam of wavelength λ , the beam width is [41]:

$$w(z) = w_0 \sqrt{1 + \left(\frac{z}{z_R}\right)^2} \quad (\text{A.2.1})$$

where $w_0 = w(0)$ denotes the beam's waist size given by $w_0^2 = \lambda z_R \pi$.

Rayleigh range The Rayleigh range z_R is defined as the distance from the origin where $w(\pm z_R) = \sqrt{2}w_0$. The confocal parameter $b = 2z_R = 2\pi w_0^2/\lambda$ denotes the depth of focus of the beam [41].

Radius of curvature $R(z)$ indicates the radius of curvature of the wave fronts comprising the beam. Its dependence on the position is given by [41]:

$$R(z) = z \left[1 + \left(\frac{z_R}{z}\right)^2 \right]. \quad (\text{A.2.2})$$

Divergence For $z \gg z_R$, the beam width $w(z)$ increases almost linearly with z . Therefor a beam divergence can be defined as [39]:

$$\frac{\Theta}{2} = \frac{w_0}{z_R} = \sqrt{\frac{\lambda}{\pi z_R}}. \quad (\text{A.2.3})$$

A.3. ABCD Law

One particularly useful property of Gaussian beams is that the effect of optical elements on the beam can be calculated by applying the ABCD law of Gaussian beam propagation. It states that in the paraxial approximation (small angular displacements θ), any optical element can be represented by a 2×2 matrix with entries A , B , C and D .

The beam is fully defined by its width $w(z)$ and its slope $dw/dz = \tan \theta \approx \theta$ such that $\mathbf{r} = (w, \theta)$ [41]. Now the beams \mathbf{r} and \mathbf{r}' , i.e. before and after passing the optical element, respectively, are related by the linear transformation [39]:

$$\mathbf{r}' = \begin{pmatrix} A & B \\ C & D \end{pmatrix} \mathbf{r}. \quad (\text{A.3.1})$$

Some commonly used ABCD matrices are given in table (A.1). Using the definition $q(z) = z - iz_R$, it can be shown that an ABCD matrix acts on the parameter $q(z)$ (which also fully describes the beam) in the following way [39]:

$$q' = \begin{pmatrix} A & B \\ C & D \end{pmatrix} \otimes q = \frac{Aq + B}{Cq + D} \quad (\text{A.3.2})$$

where q and q' describe, respectively, the parameter before and after passing the optical element.

These properties allow for beamline simulations of given experimental setups (see section 4.3).

Table A.1. Four particularly important ABCD matrices. These linear transformations can be applied sequentially in order to model an entire beam path.

Optical element	ABCD matrix
Propagation in free space over distance l	$\begin{pmatrix} 1 & l \\ 0 & 1 \end{pmatrix}$
Thin lens/spherical mirror with focal length f	$\begin{pmatrix} 1 & 0 \\ -1/f & 1 \end{pmatrix}$
Refraction at flat interface between two media with refraction indices n_1 and n_2	$\begin{pmatrix} 1 & 0 \\ 0 & n_1/n_2 \end{pmatrix}$
Refraction at curved interface between two media with refraction indices n_1 and n_2 and radius of curvature R	$\begin{pmatrix} 1 & 0 \\ \frac{n_1-n_2}{n_2 R} & n_1/n_2 \end{pmatrix}$

References

- [1] P. A. Franken, A. E. Hill, C. W. Peters, and G. Weinreich. Generation of optical harmonics. *Phys. Rev. Lett.*, 7:118–119, Aug 1961.
- [2] H. Rubens and F. Kurlbaum. Anwendung der Methode der Reststrahlen zur Prüfung des Strahlungsgesetzes. *Annalen der Physik*, 309(4):649–666, 1901.
- [3] Alexander Paarmann, Ilya Razdolski, Alexey Melnikov, Sandy Gewinner, Wieland Schöllkopf, and Martin Wolf. Second harmonic generation spectroscopy in the Reststrahl band of SiC using an infrared free-electron laser. *Applied Physics Letters*, 107(8):081101, 2015.
- [4] Wieland Schöllkopf, Sandy Gewinner, Heinz Junkes, Alexander Paarmann, Gert von Helden, Hans Bluem, and Alan M. M. Todd. The new IR and THz FEL facility at the Fritz Haber Institute in Berlin. *Proc. SPIE*, 9512:95121L–95121L–13, 2015.
- [5] Wei-Tao Liu and Y. R. Shen. Sum-frequency phonon spectroscopy on α -quartz. *Phys. Rev. B*, 78:024302, Jul 2008.
- [6] Wei-Tao Liu and Y. R. Shen. Surface vibrational modes of α -quartz(0001) probed by sum-frequency spectroscopy. *Phys. Rev. Lett.*, 101:016101, Jul 2008.
- [7] Yuen-Ron Shen. *The Principles of Nonlinear Optics*. Wiley Classics Library. Wiley-Interscience, 2003.
- [8] Guang S. He and Song H. Liu. *Physics of Nonlinear Optics*. World Scientific, 1999.
- [9] David J. Griffiths. *Introduction to Electrodynamics*. Upper Saddle River, N.J.: Prentice Hall, 3rd edition, 1999.
- [10] Paul N. Butcher and David Cotter. *The Elements of Nonlinear Optics*. Cambridge Studies in Modern Optics. Cambridge University Press, 1991.
- [11] Neil W. Ashcroft and N. David Mermin. *Solid State Physics*. Brooks/Cole, 33th edition, 1976.
- [12] Sadao Adachi. *Optical Properties of Crystalline and Amorphous Semiconductors*. Springer US, 1999.
- [13] R. H. Lyddane, R. G. Sachs, and E. Teller. On the polar vibrations of alkali halides. *Phys. Rev.*, 59:673–676, Apr 1941.

References

- [14] A. S. Barker. Transverse and longitudinal optic mode study in MgF_2 and ZnF_2 . *Phys. Rev.*, 136:A1290–A1295, Nov 1964.
- [15] Dwight W. Berreman and F. C. Unterwald. Adjusting poles and zeros of dielectric dispersion to fit Reststrahlen of PrCl_3 and LaCl_3 . *Phys. Rev.*, 174:791–799, Oct 1968.
- [16] Lev Davidovich Landau, J.S. Bell, M.J. Kearsley, L.P. Pitaevskii, E.M. Lifshitz, and J.B. Sykes. *Electrodynamics of Continuous Media*, volume 8. Elsevier, 1984.
- [17] L.P. Mosteller, Jr. and F. Wooten. Optical properties and reflectance of uniaxial absorbing crystals. *J. Opt. Soc. Am.*, 58(4):511–518, Apr 1968.
- [18] Y.R. Shen. Optical second harmonic generation at interfaces. *Annual Review of Physical Chemistry*, 40(1):327–350, 1989.
- [19] C. Flytzanis. Infrared dispersion of second-order electric susceptibilities in semiconducting compounds. *Phys. Rev. B*, 6:1264–1290, Aug 1972.
- [20] W. L. Faust and Charles H. Henry. Mixing of Visible and Near-Resonance Infrared Light in GaP. *Phys. Rev. Lett.*, 17:1265–1268, Dec 1966.
- [21] W. L. Faust, C. H. Henry, and R. H. Eick. Dispersion in the Nonlinear Susceptibility of GaP near the Reststrahl Band. *Phys. Rev.*, 173:781–786, Sep 1968.
- [22] T. Dekorsy, V. A. Yakovlev, W. Seidel, M. Helm, and F. Keilmann. Infrared-phonon-polariton resonance of the nonlinear susceptibility in GaAs. *Phys. Rev. Lett.*, 90:055508, Feb 2003.
- [23] Eric Roman, Jonathan R. Yates, Marek Veithen, David Vanderbilt, and Ivo Souza. *Ab initio* study of the nonlinear optics of III-V semiconductors in the terahertz regime. *Phys. Rev. B*, 74:245204, Dec 2006.
- [24] F. Gervais and B. Piriou. Temperature dependence of transverse and longitudinal optic modes in the α and β phases of quartz. *Phys. Rev. B*, 11:3944–3950, May 1975.
- [25] Koichi Momma and Fujio Izumi. *VESTA3* for three-dimensional visualization of crystal, volumetric and morphology data. *Journal of Applied Crystallography*, 44(6):1272–1276, Dec 2011.
- [26] A.F. Wright and M.S. Lehmann. The structure of quartz at 25 and 590 °C determined by neutron diffraction. *Journal of Solid State Chemistry*, 36(3):371 – 380, 1981.
- [27] J. F. Scott and S. P. S. Porto. Longitudinal and transverse optical lattice vibrations in quartz. *Phys. Rev.*, 161:903–910, Sep 1967.

- [28] D. Strauch and B. Dorner. Lattice dynamics of α -quartz: I. Experiment. *Journal of Physics: Condensed Matter*, 5(34):6149, 1993.
- [29] Toshiyuki Shiozawa. *Classical Relativistic Electrodynamics – Theory of Light Emission and Application to Free Electron Lasers*. Springer-Verlag Berlin Heidelberg, 2004.
- [30] Sándor Varró, editor. *Free Electron Lasers*. InTech, 2012.
- [31] H. Motz. Applications of the radiation from fast electron beams. *Journal of Applied Physics*, 22(5):527–535, 1951.
- [32] Luis R. Elias, William M. Fairbank, John M. J. Madey, H. Alan Schwettman, and Todd I. Smith. Observation of stimulated emission of radiation by relativistic electrons in a spatially periodic transverse magnetic field. *Phys. Rev. Lett.*, 36:717–720, Mar 1976.
- [33] D. A. G. Deacon, L. R. Elias, J. M. J. Madey, G. J. Ramian, H. A. Schwettman, and T. I. Smith. First operation of a free-electron laser. *Phys. Rev. Lett.*, 38:892–894, Apr 1977.
- [34] Neil Thompson. Introduction to Free Electron Lasers. ASTeC - Accelerator Science and Technology Centre, 2015.
- [35] W. Bragg and R. E. Gibbs. The structure of α and β quartz. *Proceedings of the Royal Society of London. Series A, Containing Papers of a Mathematical and Physical Character*, 109(751):405–427, 1925.
- [36] R.W.G. Wyckoff. Crystal structure of high temperature (β -) modification of quartz. *American Journal of Science*, (62):101–112, 1926.
- [37] Florence Bart and Martine Gautier. A LEED study of the (0001) α -quartz surface reconstruction. *Surface Science*, 311(1):L671 – L676, 1994.
- [38] W. Steurer, A. Apfelter, M. Koch, T. Sarlat, E. Søndergård, W.E. Ernst, and B. Holst. The structure of the α -quartz (0001) surface investigated using helium atom scattering and atomic force microscopy. *Surface Science*, 601(18):4407 – 4411, 2007. Proceedings of the 24th European Conference on Surface Science.
- [39] Dieter Meschede. *Optik, Licht und Laser*. Vieweg+Teubner, 3rd edition, 2008.
- [40] Anthony E. Siegmann. *Lasers*. University Science Books, 1986.
- [41] Orazio Svelto. *Principles of Lasers*. Springer US, 5th edition, 2010.

List of Figures

1.1.	Energy diagrams for sum frequency generation and second harmonic generation.	2
2.1.	Dielectric function around a phonon resonance and refractive index.	7
2.2.	Schematic of wave vectors for reflection and transmission.	9
2.3.	Crystal lattice structure of α -quartz.	16
2.4.	Experimental reflectivity data from Gervais et al. [24].	16
2.5.	Phonon dispersion of α -quartz measured with neutron scattering.	18
2.6.	Basic setup of a free-electron laser.	19
2.7.	Scheme of the center plane of an undulator.	20
2.8.	An electron's orbit through the center plane of an undulator.	21
2.9.	Schematic of microbunching.	22
3.1.	Simulated spectra of the real part of the dielectric function.	25
3.2.	Reflectivity spectra for four different temperatures.	26
3.3.	Simulated spectra of the Fresnel-corrected reflectivity.	27
3.4.	Schematic of the non-collinear second harmonic generation in reflection.	29
3.5.	Plots of the calculated azimuthal intensity model.	31
4.1.	Setup of the FHI FEL.	33
4.2.	Pulse structure of the FHI FEL.	35
4.3.	Schematic of the SHG autocorrelator setup.	35
4.4.	Schematic of the probe heater.	37
4.5.	Beamline simulation for the SHG experiment.	38
4.6.	Intensity map of the excitation beam profiles.	39
5.1.	SHG spectrum at room temperature.	42
5.2.	Temperature dependence of the SHG signal.	44
5.3.	Azimuthal SHG scans.	46
5.4.	Temperature-dependent azimuthal SHG scans.	48
5.5.	Reflectivity spectra at room temperature.	51
5.6.	Temperature dependence of the reflectivity.	52
6.1.	Temperature dependence of SHG and reflectivity intensities integrated over the entire spectral range.	56
6.2.	Temperature dependence of SHG and reflectivity.	58
A.1.	A Gaussian beam's width profile near the beam waist.	64

Acknowledgements

First and foremost I want to thank Martin Wolf for supervising this thesis and giving me the opportunity to work at the FHI's Department of Physical Chemistry which was – and still is – a very inspiring and motivating experience.

I am extremely thankful for Alexander Paarmann's guidance and support throughout this time. His passion for science, commitment and outstanding teaching skills are of incomparable importance to my work at the Lattice Dynamics group and make this project a joy to work on as well as an invaluable lesson. I am looking forward to the years to come as a doctoral student in his group.

Furthermore, I would also like to thank the Lattice Dynamics group as a whole: Ilya, Riko, Nikolai and in particular Christian who deserves a special mention for his incredible helpfulness at all times, especially during my first weeks at the institute.

Many thanks are also due to the FEL team, Wieland and Sandy, who made sure that the machine always worked as well as it did and without whom the experiments in this work would not have been possible.

I was very happy to learn that the second supervisor of this thesis would be Albrecht Lindinger who has kindled my interest for nonlinear optics when I was working in his research group for my bachelor's thesis. I have always appreciated the friendly contact which has persisted since then.

Finally, I want to say thank you to my family and friends who – with their endless love and support – not only contributed to this thesis but also to my life as a whole. Danke!